IEEE Access
Multidisciplinary ⋮ Rapid Review ⋮ Open Access Journal

Received 23 February 2024, accepted 18 March 2024, date of publication 21 March 2024, date of current version 28 March 2024.

Digital Object Identifier 10.1109/ACCESS.2024.3380201

SURVEY

Directional Wave Scattering Distribution Modes Analysis and Synthesis of Random Ocean Media Roughness for SAR Electromagnetic Interactions Using Feature Fusion in Dynamic Sea States: A Survey

IMAN HEIDARPOUR SHAHREZAEI, (Member, IEEE), AND HYUN-CHEOL KIM, (Member, IEEE)
Center of Remote Sensing and GIS, Korea Polar Research Institute (KOPRI), Incheon 21990, South Korea

Corresponding author: Hyun-Cheol Kim (kimhc@kopri.re.kr)

This work was supported by Korea Polar Research Institute (KOPRI) (Study on Remote Sensing for Quantitative Analysis of Changes in the Arctic Cryosphere) under Grant PE24040.

ABSTRACT Ocean waves have long been a research topic, and numerous formulas of the ocean wave spectrum have been widely developed to provide new prospects for ocean experiments and the advancement of radar probing. Nonetheless, the wave spectra developed by researchers fall short of the standards set by remote sensing specialists, mainly due to the limitation of capturing the surface roughness influenced by both short and long waves, prompting ongoing efforts to develop a model covering a diverse scale of wavenumbers in the absence of a generally recognized reference formula. In response, a standard two-scale formulation of wave frequency spectra (WFS) was introduced, where wave height and spectral peak period are determined by sea state. The proposed composite WFS holds the potential to incorporate directional spreading, contributing to the angular distribution of ocean wave energy in the form of directional WFS, making it applicable for ocean modeling. In an effort to investigate directionality effects, an array of well-established spreading functions, including cosine-squared, half-cosine 2s, parameterized half-cosine 2s, hyperbolic secant-squared, and composite structured functions, has been developed here for numerical modeling of random ocean media (ROM) surface roughness and synthesized for their spectral scattering distribution mode, encompassing scattering pattern, scattering orientation, and fractal roughness properties. Nonetheless, the generated ROM models, each varying due to inherent limitations in directional WFS formulation and numerical approximations, demonstrate indeterminacy and unpredictability in surface features, posing challenges for accurately synthesizing ROM roughness patterns. These challenges intensify under varying sea states and different directional WFS formulas, leading to a situation where no single synthesized composite ROM model consistently outperforms the others, rendering them imprecise frameworks for analyzing roughness patterns and investigating texture electromagnetic interactions within the realm of remote sensing. As an approach, a pattern-sensitive fusion method is proposed, employing a multi-scale transform domain (MTD) fusion scheme that leverages the learning potential of a deep super resolution network. The objective is to fuse the reconstructed ROM roughness models, generating an optimal roughness while maintaining their scattering pattern, scattering orientation, and dominant directionality, pivotal for texture consistency and, consequently, the backscattering properties from the synthetic aperture radar (SAR) viewpoint. To validate the reliability of ROM modeling and its roughness synthesis, including the texture fusion and raw data generation, a comprehensive objective quality assessment technique is utilized. These

The associate editor coordinating the review of this manuscript and approving it for publication was Xuebo Zhang.

assessments demonstrate the complete consistency of the simulation results with the underlying spectral theory, highlighting their potential contribution to projects related to ocean radar probing and remote sensing.

INDEX TERMS Directional wave frequency spectrum, fractal fusion, random ocean media, sea state, synthetic aperture radar.

I. INTRODUCTION

The description of an ocean surface roughness, including asymmetric surface effects, has been studied both theoretically and experimentally [1], [2], [3]. To a first approximation, an ocean surface can be considered as a linear superposition of statistically independent time records of free waves described by their energy spectrum [4], [5]; however, the non-linearity of wave interactions [6], such as surf beats [7], wave breaking [8], and energy transfer between wave components [9], which are important in later stages of wave development and determine the equilibrium state [10], [11], could not be accounted for [12], [13], and [14]. Therefore, statistical formulations utilizing high-order energy cumulants of the scattering process in the presence of wind-waves have been used to describe the continuous interactions and energy exchanges, comprising the ocean and atmosphere, hereinafter referred to as random ocean media (ROM) [15], [16]. The analysis of the ROM energy momentum phenomenon involves complex variables and necessitates considerable idealizations, which can be done in one of two methods [17]. The first method is a dissipative mechanism that considers the breaking of free surface waves through energy exchange between the atmosphere and the ocean [18], while the second method involves wind-driven surface synthesis based on spectral scattering mechanisms [19]. The two methods take distinct approaches, and the relative precedence of spectral and dissipative mechanisms in the evolution of ROM is uncertain [20]; however, the spectral approach tends to broaden the directional spread of wavefield scattering and aids in the prediction of energy fraction induced by modulation effects at the atmosphere-ocean interface, whereas dissipation does not [17]. Taking this into account, and given the random nature of wind-generated waves, focusing on statistical scattering properties of wavefield has been deemed a suitable approach for studying the evolution of ROM [21], [22], [23], [24], [25], [26]. Within this context, there is a wealth of formulations detailing wave frequency spectra (WFS) that describe ocean wave energy scatterings, contributing to the description of ROM [27], [28], [29], [30], [31]; nonetheless, due to time-evolving oceanic conditions, the full range of wavenumber investigation remains unreconciled both theoretically and empirically [32], [33], necessitating a broad range of spectral synthesis based on physical oceanic conditions to address ROM's spatiotemporal scattering characteristics [34], [35], [36].

In essence, the spectral scattering formulation of ROM can be divided into two categories, namely approximate experimental formulations and numerical methods [35], [37]. Experimental methods are of great significance in numerous studies as they offer physical insights that cannot be solely provided by the theory of wave scatterings [38], demonstrating the impact of surface parameter variations on scattering properties [39], [40]. However, the major drawbacks of these empirical formulations lie in their absence of domain categorization and limited evaluation scenarios [41], [42], as no field experiments have been conducted to measure the entire wavelength range to date and there is no widely accepted WFS formula that covers the entire domain [43]. To address these limitations and offer validations, numerical methods covering a wide range of wavelengths have been introduced, each focusing on solving a specific problem [44], [45], [46], [47]. However, given the approximate nature of all numerical methods [48], the modeling procedure must strike a balance between accuracy, complexity, and dimensionality [49]. Specifically, for reliable numerical modeling of ROM, it is crucial to effectively characterize the stochastic scattering properties of these nondeterministic media by incorporating a statistical distribution of spectral components that reflects the trade-off between approximation and dimensionality [30], [39], [42], [46], [47], [48], [49], [50], [51]. In this context, numerical models are utilized to explore the distinctive physical characteristics of ROM, particularly in surface roughness patterns, a phenomenon challenging to fully replicate through experimental formulations, especially amidst wind-waves and specific oceanic conditions, commonly referred to as sea states [44], [45], [46], [47], [52], [53], [54]. As a result, numerical modeling of ocean surface roughness involves analyzing spectral scattering contributions from the ROM's physical state and dynamics [30], [55], characterized by the statistical distribution of WFS under various sea states [37], [55], [56], [57], determined by wind speed and direction [52], [55], [58], [59], holding scientific significance, especially in ocean probing [59], [60], [61], [62].

It is worth noting that, despite anecdotal evidence either on the sole use of numerical methods or on data interpretations of ocean surface [38], [40], [47], [56], [58], [62], [63], [64], [65], a survey article addressing the numerical modeling of ROM roughness and its structural interpretation [66], [67], with a focus on the stochastic distribution of WFS under varying sea state conditions, has yet to be a published. More specifically, although most studies have focused on the physical formulation of WFS [64], [68], [69], [70], addressing specific problems in distinct domains primarily using either 1D formulas or 2D simulations [71], [72], [73], there is currently a gap in the literature regarding a comprehensive survey on the 3D modeling of ROM through WFS synthesis and the analysis of roughness patterns in response to sea states [37]. In this context, the WFS formula proves more

effective in a two-scale format, referred to as a composite spectrum [74], incorporating major ocean wave modulation effects [37], wideband resonant modulation impacts [37], [63], and associated filtering effects [63], all crucial for determining the spectral distribution and the structural interpretation of the ROM [75], [76]. Thus, conducting a survey on modeling of ROM using two-scale WFS has the potential to offer valuable insight into the physical and structural properties of the ocean surface, with implications for various ocean remote sensing interpretations [25], [26], [43], [48], [50], [54], [58], [59], [60], [61], [62], [64], [65], [73], [74], [77]. Moreover, by incorporating these roughness profiles into synthetic aperture radar (SAR) observations [60], [73], [78], [79], investigating their textural properties [77], [80], [81], and analyzing relevant backscattering properties [82], [83], [84], [85], valuable results can be obtained through composite ROM models that have yet to be reported in existing literature [20], [25], [35], [37], [43], [48], [49], [52], [53], [54], [55], [56], [57], [58], [59], [61], [62], [63], [64], [70], [74], [75], [76], [77], [78], [79], [80], [83], [84], [85], [86], [87], [88], [89], [90], [91], [92], [93].

In the context of remote sensing and numerical modeling for composite ROM surface roughness, Elfouhaily et al. introduced a unified WFS accurately depicting gravity-capillary wave curvature dynamics as measured in the field [94], aligning with the high-frequency regime analytical format [91], [93], [94], and yielding wind-dependent results through the integration of the wave slope spectrum [95], [96], [97], [98]. Importantly, their two-scale WFS functions as a unified curvature spectrum in the wavenumber domain [37], [74], incorporating wave age dependence in both long and short wind-waves, and indicating aligned wind and wave directions [94], [99]. This suggests that the formulated WFS considers physical oceanic condition, breaking dissipations, frictions, and nonlinear interactions [100], resulting in a finite-depth asymptotic condition that offers valuable insights into wind-wave generation and energy distribution [100], [101]. In the context of this highly dynamic medium, wind-waves exhibit multidirectional randomness and gain energy with increasing wind speed, duration, and fetch size [102], leading to the alignment of the peak wave direction with the wind direction and subsequent alterations in the distribution of energy [103]. This underscores the importance of the angular distribution of ocean waves within the realm of wave kinematics [104], characterizing the directional spreading of wave energy and emphasizing the influence of sea states on angular wave distributions, commonly known as angular spreading [83], [84], [103]. Therefore, further analysis is required to investigate the directional distribution of Elfouhaily's WFS [74], [99], [105], with a specific focus on directional scatterings in the form of directional WFS [106], [107], [108], resulting from the product of the Elfouhaily's spectrum and an angular spreading function [102], [105], with the spreading function available in various forms [43], [109], [110], [111], [112], [113].

As an approach, this survey aims to explore a forward statistical surface roughness modeling of ROM using a series of well-established spreading functions in conjunction with the Elfouhaily's two-scale WFS, hereinafter referred to as directional two-scale WFS, to synthesize composite ROM surface roughness under varying sea state conditions [114], [115], [116], which have yet to be reported [6], [15], [23], [25], [30], [43], [44], [49], [52], [55], [56], [57], [58], [59], [63], [65], [81], [99], [102], [108], [113]. To achieve this, the wavenumber-domain is employed to express ROM scattering characteristics, incorporating frequency-dependent components derived from time-evolving sea states [94]. This approach captures the maximum impact of hydrodynamic modulations and atmospheric instabilities arising from wind-wave interactions [43], [53], while also emphasizing the contribution of shear and divergence of surface currents as directional roughness features, especially in the presence of wind fields [9], [59], [117], [118]. Building upon the composite roughness modeling as a function of directional WFS, the reconstructed ROM models are further analyzed by characterizing their surface height profiles to account for variations in sea states, including changes in wind speed and deviations in wind direction [52], [62], [118], [119], [120], [121]. This analysis provides valuable structural insight into ocean hydrodynamics and directional wind-waves scatterings, which are of significance for radar probing, particularly SARs [120], [121], [122]. The survey extends beyond ROM modeling, encompassing the synthesis of ocean surface roughness and its electromagnetic interactions, with a specific focus on the intricate dynamics of texture structures as manifested through scattering patterns, scattering orientations, and variations in wave height details, known as roughness fluctuations [43], [48], [50], [63], [66], [77], [82], [91], [92], [113], [118], [121], [123]. Given the dependency of directional WFS formulation on both spreading function and its boundary conditions, which includes the effects of sea states [84], [108], [112], no ROM model generated thus far outperforms others in terms of representing reference roughness pattern and texture characteristics [45], [49], [56], [63], [65], [77], [88], [89], [93], [99], [103], [108], [113], [117], [120]. To address this limitation, a multi-scale transform domain (MTD) fusion method is proposed [124], [125], [126], [127], incorporating a convolutional neural network (CNN) [128], [129], enabling the reconstruction of a fused roughness model independent of spreading functions as a reference ROM [50], [80], [103], [129], and facilitating the generation of an optimized SAR raw data [59], [60], [73], [74], [77], [80], [83], [84], [85], [86], [87], [93], [106], [107], [119], [121].

To the best of the authors' knowledge, this survey presents an end-to-end approach to SAR remote sensing of the ocean, incorporating a composite roughness modeling of ROM based on directional two-scale WFS formulation under varying sea state conditions that has yet to be reported [9], [29], [30], [37], [44], [45], [46], [52], [55], [59], [61], [63],

[65], [74], [80], [87], [91], [92], [99], [106], [113], [114], [115], [117]. It encompasses a range of surveys, including numerical modeling of ROM, synthesis of surface texture, analysis of roughness patterns and fractal fluctuations, investigation of SAR texture electromagnetic interactions, and the generation of an optimal reference roughness model. The proposed approach reduces the reliance on ocean empirical approximations and field observations [11], [35], [38], as well as the limitations of formulations [6], [22], such as dimensionality [30], [50], [55], large-scale formulations [3], [41], modulation effects [53], [68], [74], stochastic distributions [19], [42], [76], and wavenumber complexities [36], [47], [101]. In a broader context, this research extends the groundwork laid by [9], [12], [24], [25], [26], [27], [29], [30], [34], [37], [42], [46], [48], [49], [50], [55], [56], [57], [58], [59], [60], [61], [62], [64], [65], [67], [68], [73], [74], [75], [76], [77], [78], [80], [82], [86], [87], [91], [92], [93], [94], [96], [98], [100], [103], [106], [113], [114], [117], [119], [121], [124], [125], [126], [127], [128], [129], [130], and [131], addressing gaps in the modeling of composite ROM, synthesis of texture in response to sea states, and investigation of directionality effects through spreading functions implementation. Moreover, the survey introduces an optimal reference ROM model generation through MTD fusion, employing CNN, and investigates its impacts on the backscattering profile, followed by objective assessment.

This paper is organized as follows. In Section. II the concepts and formulations of omnidirectional two-scale WFS are discussed, including simulations comparing it to conventional WFS at different wind speeds. Section. III, focuses on the directional approach toward WFS formulation, specifically highlighting the implementation of a directional two-scale WFS through a series of well-known spreading functions. Section. IV covers the numerical modeling procedure for ROM, while Section. V presents simulation results for the introduced directional WFS functions under varying sea state conditions. Furthermore, this section investigates the structural properties of texture in relation to directionality effects, analyzing aspects such as scattering pattern, scattering orientation, and fractal roughness fluctuations. Section. VI, highlights the importance of a reference ROM model and introduces the concept of optimal roughness MTD fusion using CNN, followed by and inverse problem solution for extracting SAR electromagnetic interaction profiles, supported by simulation results and objective verification scenarios. In conclusion, Section. VII offers the concluding remarks for this survey article.

II. OMNIDIRECTIONAL TWO-SCALEWFS CONCEPT AND APPROACHES

Due to the lack of a unified and widely recognized wave model [89], ocean WFS is marked by a variety of forms, each showing notable discrepancies due to the utilization of different scattering formulations [43]. Consequently, it is crucial to reevaluate and replace arbitrary parameters with fixed values to improve the spectral response [103], facilitating the developments of a more unified scattering formula capable of accommodating both long-wave and short-wave curvature spectrums in parallel [89]. To address this, the application of a two-scale WFS formulation, which can be easily extended to incorporate angular energy distribution across varying sea states, holds significant importance [103]. In this context, Elfouhaily's formula, which integrates two spectral regimes, has been introduced [74], [87]. To discern the unidirectional spectral dependency on angular distribution [109], [110], [111], [112], [113], the formulated WFS incorporates a matching angular spreading function [43], [94]. This allows for effective evaluation of the directional characteristics of the wavefield within the fetch [16], resulting in a unified WFS for modeling [53], [94]. Hence, this section will delineate the formulation of the Elfouhaily's two-scale WFS, encompassing its key components, including the long-wave and short-wave curvature spectrums.

A. LOW-FREQUENCY CURVATURE SPECTRUM

The low-wavenumber components of the two-scale WFS, which represent long-waves with wavenumbers up to 10 times the spectral peak k_p, are expressed as [94], [132]:

$$B_l = 0.5\alpha_p \frac{c_p}{c} F_p \tag{1}$$

where, α_p is the generalized equilibrium range parameter for long-waves that is dependent on the dimensionless inverse wave age parameter Ω [10], [133], c is the wave phase speed, $c_p = c(k_p)$ is the phase speed at the spectral peak or the dominant long-wave, and F_p is the long-wave side effects function as follows:

$$F_p = L_p J_p \exp\left\{-\frac{\Omega}{\sqrt{10}}\left[\sqrt{\frac{k}{k_p}} - 1\right]\right\} \tag{2}$$

With

$$L_p = \exp\left[-1.25\left(k/k_p\right)^2\right] \tag{3}$$

$$J_p = \gamma^{\Gamma} \tag{4}$$

$$\alpha_p = 0.006\Omega_c^{0.55} \tag{5}$$

$$\Omega = U_{10}/c_p \tag{6}$$

$$\Omega_c = \Omega\cos\left(\bar{\theta}\right) \tag{7}$$

$$\begin{cases} \gamma = 1.7, & 0.84 < \Omega_c < 1 \\ \gamma = 1.7 + 6\log\left(\Omega_c\right), & 1 < \Omega_c < 5 \end{cases} \tag{8}$$

$$\Gamma = \exp\left\{-\frac{\left(\sqrt{\frac{k}{k_p}} - 1\right)^2}{2\sigma^2}\right\} \tag{9}$$

$$\sigma = 0.08\left[1 + 4\Omega_c^{-3}\right] \tag{10}$$

where, L_p represents the shape spectrum, J_p is the peak enhancement factor, U_{10} is the wind speed at $10m$ above the ocean surface, and $\bar{\theta}$ denotes the mean wind direction, indicating the alignment between the wind and the dominant waves at the spectral peak. The third term in (2) accounts

for a wind-generated wavefield property, serving as an additional cutoff that limit the energy-containing part of the spectrum to less than $10k_p$ [134]. As a result, the curvature spectrum oscillates at $10k_p$ [96], indicating that steep mechanically generated waves produce parasitic capillary waves in the absence of wind [134]. This highlights that long-waves, referred to as low-frequency curvature spectrum, are dependent on wave-age and fetch [94]. Consequently, the dimensionless significant wave height can be calculated as a function of fetch, particularly the long fetch, which aligns with other spectral models such as Pierson-Moskowitz (PM) [32], [57], [135].

B. HIGH-FREQUENCY CURVATURE SPECTRUM

Since the spectral form appeared to be independent of the fetch in the gravity-capillary range [136], [137], the short-wave curvature spectrum, representing the high-wavenumber components of the two-scale WFS, can be expressed as [138]:

$$B_h = 0.5\alpha_m \frac{c_m}{c} F_m \tag{11}$$

$$\alpha_m = \begin{cases} 10^{-2}\left[1 + \ln\left(u^*/c_m\right)\right], & u^* < c_m \\ 10^{-2}\left[1 + 3\ln\left(u^*/c_m\right)\right], & u^* > c_m \end{cases} \tag{12}$$

where, α_m represents the generalized equilibrium range parameter for short waves in the two-regime, which depends on the dimensionless parameter (u^*/c_m), where u^* denotes the friction velocity at the surface, and c_m represents the minimum phase speed at the wavenumber k_m associated with a gravity-capillary peak in the spectrum, defined as:

$$c_m = \sqrt{2g/k_m} \tag{13}$$

where, g denotes the acceleration due to gravity, and F_m in (11) stands for the short-wave side effect function, and can be expressed as:

$$F_m = \exp\left\{-0.25\left[\frac{k}{k_m} - 1\right]^2\right\} \tag{14}$$

The exponential factor in (14) addresses both the viscous cutoff and the gravity-capillary wave bandwidth. The logarithmic behavior of α_m in the bimodal formulation is influenced by the ratio of wind friction velocity to wave phase speed [139], indicating the comparable importance of spectral flux divergence, wind input, and dissipation in shaping the short-wave spectrum. Specifically, wind energy input primarily occurs at scales with concentrated energy, whereas dissipation becomes more significant at higher wavenumbers. This interaction between input and dissipation influences the growth rate and formation of the short-scale spectrum, making a transition from hydrodynamically smooth to rough flow as small-scale wave breaking intensifies, ultimately leading to a noticeable saturation of the curvature spectrum at high speeds [140].

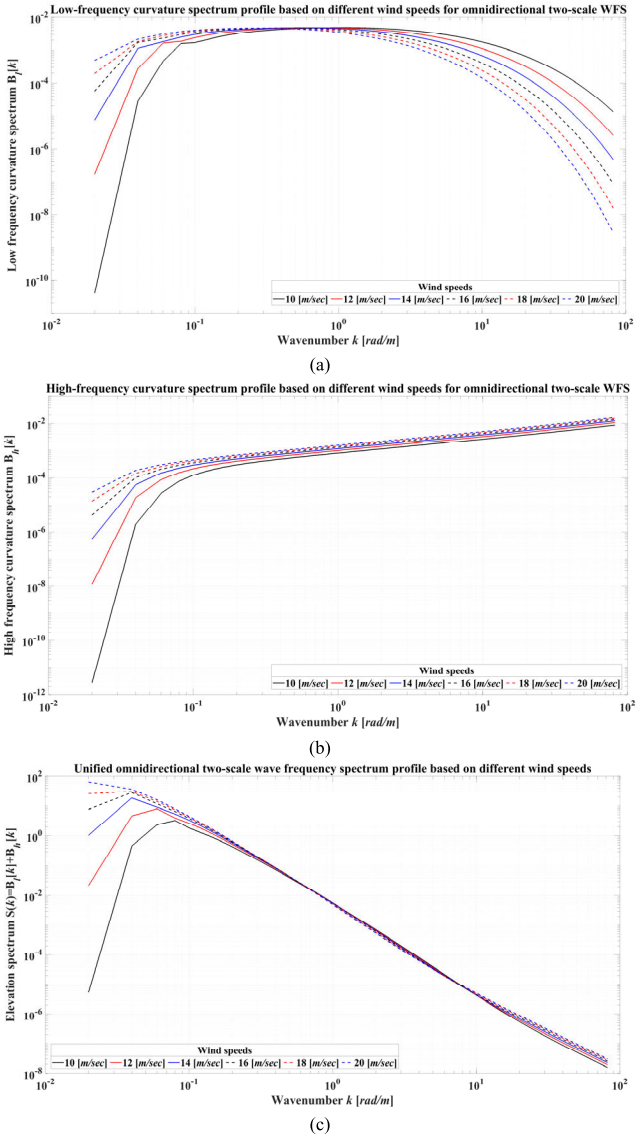

FIGURE 1. Wavenumber simulation of the Elfouhaily's two-scale WFS based on different wind speeds from 10 m/s to 20 m/s with a 2 m/s step (a) low-frequency curvature spectrum (b) high-frequency curvature spectrum (c) elevation spectrum.

C. OMNIDIRECTIONAL TWO-SCALE WFS APPROACH

When a steady wind persists over a long fetch of deep water, it gives rise to an equilibrium wave spectrum that mirrors the Maxwellian distribution of velocities in a uniform medium, representing a state of maximum entropy [43], [141], and facilitating the development of a WFS formulation [142]. However, achieving a fully consistent WFS across the entire wavelength range is idealistic and constrained by the limitations of time, location, and methodology, which hinders the development of a coherent formula [43]. To address this, an omnidirectional two-scale WFS is introduced [94], providing a unified algebraic representation of ROM spectral scatterings, which resulted in achieving satisfactory agreement with data in hydrodynamic and energy scatterings,

as follows [94], [103]:

$$S(k) = k^{-3}[B_l + B_h] \tag{15}$$

where, $S(k)$ denotes the elevation spectrum, with subscripts l and h indicating low and high-frequencies respectively, and B referring to the corresponding curvature spectra. It is important to highlight that the wavenumber representation of $S(k)$ exhibits physical consistency, aligning with the minimum phase speed at which the combined impacts of wind-induced hydrodynamic and aerodynamic modulations by longer waves exert the most significant influence [53]. This also enables the spectrum to account for wind and frequency variations in wave scatterings [143], indicating that the curvature spectra and the formulated elevation spectrum are adept at capturing wave height variations while being influenced by wind speeds [103]. The simulation results in Fig. 1, depicts the spectral components of B_l, B_h, and the resultant two-scale $S(k)$ over a wide range of wavenumbers based on different wind speeds. As can be deduced, Fig. 1(a) illustrates the spectral components of B_l, which are impacted by wave-age and fetch, resulting in a spectrum divergence as both wavenumber and wind speed increase. This divergence is accompanied by the appearance of a dominant peak corresponding to the highest energy wave frequency, typically characterizing the energy distribution of larger, slower-moving waves [94]. Similarly, in Fig. 1(b), the high-wavenumber components of B_h are shown, exhibiting a predominantly consistent pattern at high wavenumbers, accompanied by a distinct saturation of the curvature spectrum under high wind speeds [103]. These wave components tend to display sharper and more tightly spaced features within the spectrum, which is a critical factor for capturing fine details and roughness fluctuations in wave height patterns, particularly in response to strong winds and shorter-period waves [94].

Accordingly, Fig. 1(c), representing the algebraic two-scale presentation of WFS, offers insights into the characteristics of the elevation spectrum in (15), indicating wave growth and energy dissipation in the presence of extreme wind conditions, particularly at high wavenumbers. The results affirm the effectiveness of composite formulation for wave regimes in capturing features across a wide range of scales influenced by wind speeds. They emphasize the intertwined impacts of both the long-wave spectrum characterizing fetch-limited wind waves and the short-wave spectrum representing capillary-gravity waves, with the dynamics of these components intimately coupled [103]. In other words, the validity of two-scale WFS extends across the entire wavenumber ranges, capturing diverse interactions between wind and waves at both low and high wavelengths in all directions, thus referred to as the unified omnidirectional two-scale WFS.

While two-scale $S(k)$ excels at capturing intricate ROM details and their complex interactions between wind and waves across a wide range of wavelengths, not all WFS formulations possess the same level of detail. For instance, the

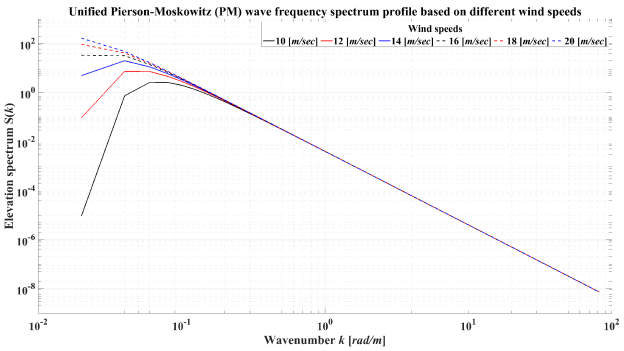

FIGURE 2. Wavenumber simulation of the Pierson-Moskowitz WFS based on different wind speeds from 10 m/s to 20 m/s with a 2 m/s step.

PM model, another widely recognized formulation, mainly characterizes the spectrum of fully developed wind-generated waves using a uniscale spectral structure of [144]:

$$S(k) = \frac{\alpha}{2\pi k^4} \exp\left\{-\left(\frac{\beta g^2}{k^2 U^4}\right)\right\} \tag{16}$$

where, $S(k)$ represents the PM spectra, with constants α =0.008 and β= 0.74, and U represents the wind speed. It is important to note that the PM spectrum relies on particular idealizations and assumptions related to wave behavior, valid under the steady wave conditions with constant wind speed over a specific distance, primarily driven by local winds, and without significant interactions with the ocean. These constraints potentially limit its ability to accurately represent complex ocean wave modulations in intricate sea conditions characterized by high wind speeds, crucial for capturing wave interactions and the fine details of wave patterns. Figure. 2 demonstrates the PM wave frequency spectra over the same wavenumber domain as used in Fig.1. As can be inferred from the results in Figs. 1 and 2, both spectral models display a concentration of energy around their respective peaks, with a rapid decrease in energy as one moves away from the peak of the spectrum [140]. As the wind speed increases, the spectrum experiences a gradual increase in its peak, and this increase occurs at smaller wavenumbers. This trend suggests that with higher wind speeds, the energy within the wave spectrum intensifies, becoming more focused on longer waves characterized by long wavelengths [43]. In the high wavenumber domain, the PM spectrum remains relatively stable, showing minimal deviations as wind speed increases. In contrast, the two-scale spectrum experiences an increment in the energy of its short-wave components as wind speed rises. This suggests that the Elfouhaily WFS is built upon the foundation of the PM, with additional influence of the short-waves being incorporated into the components [140].

Furthermore, within the low-wavenumber range, both the two-scale spectrum and the PM spectrum exhibited limited variations as wind speed increased. However, in the high wavenumber domain, as the wind speed increased, the energy of the short-wave components in the two-scale spectrum progressively intensified and shifted towards larger wavenumbers, indicating its capability in capturing a more

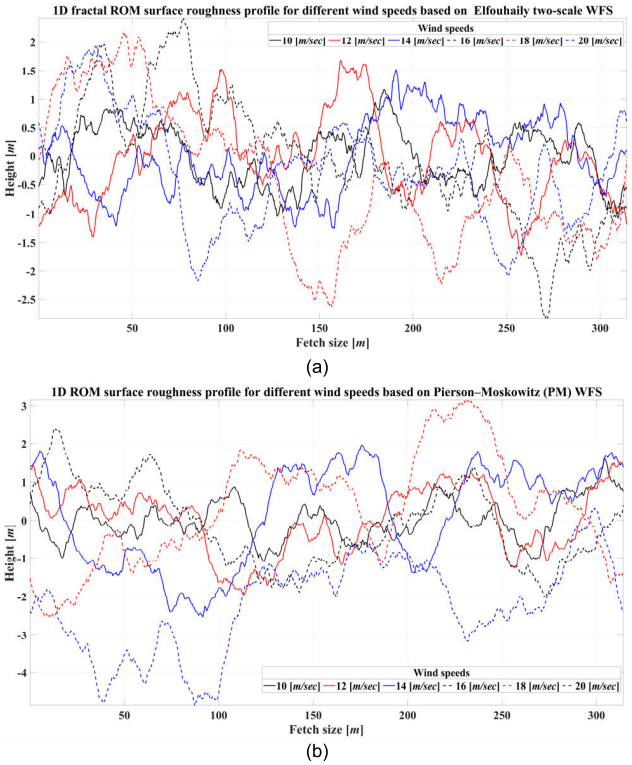

FIGURE 3. 1D ROM surface roughness profiles under different wind speeds ranging from 10 m/s to 20 m/s with a 2 m/s step based on the (a) Elfouhaily two-scale WFS (b) PM spectrum.

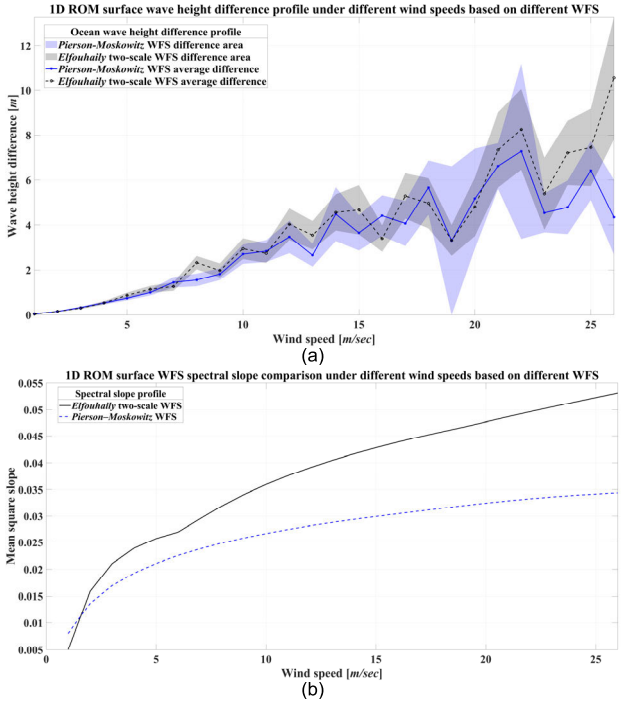

FIGURE 4. 1D ROM roughness profile comparisons between Elfouhaily and PM spectrums (a) wave height variance (b) WFS spectral slope.

extensive set of ocean wave height information compared to the PM spectrum [140]. In essence, the two-scale spectrum is regarded as a more comprehensive wavenumber spectrum, capable of accommodating a broader range of wave scattering information in high wind speed conditions. This makes Elfouhaily's model suitable for ROM roughness profile extraction, representing diverse sea wave types and wind speeds, while the PM spectrum consistent spectral shape and limited sensitivity to short-wave variations in the high-wavenumber domain make it less accurate for representing complex oceanic conditions characterized by high wind speeds [140]. This distinction is particularly notable in applications related to ROM radar observations and the study of fine roughness details [43], [92]. To further explore this, simulations and evaluations of ROM surface roughness profiles were conducted based on the two-scale WFS and the PM spectrum under the wind speed conditions depicted in Figs. 1 and 2. The results presented in Fig. 3 depict ROM surface profiles formed through the superposition of wave harmonics characterized by random phase. Amplitudes as functions of spatial coordinates were obtained using a numerical simulation approach [37], [46]. This involves filtering Gaussian random noise in spatial coordinates using the square root of spectra. The filtered spectrum is then inverse Fourier transformed to obtain amplitude variations in spatial coordinates. This method ensures that the amplitude information is represented with respect to spatial coordinates, providing a more comprehensive understanding of the ROM surface profiles. Notably, the selection of specific parameters, including the capillary peak wavenumber value, fetch constant, and dimensional fetch value, adheres to the principles of the two-scale spectrum structure [94]. As can be deduced, each wind speed level manifests a unique surface roughness profile characterized by differences in wave heights and fluctuations.

Lower wind speeds yield reduced wave heights and smaller roughness fluctuations, whereas higher wind speeds produce larger wave heights with more significant fluctuations. The provided results are further illustrated in Fig.4, highlighting surface roughness fluctuations for both the two-scale WFS and PM spectrum, as well as their average wave heights. It is evident that higher wind speeds correspond to increased average wave heights and more significant wave height fluctuations, representing the difference between maximum and minimum ocean wave heights at that specific wind speed. This difference is particularly pronounced in Elfouhaily's spectrum compared to PM, owing to the heightened energy of short-wave components in the high-wavenumber domain, resulting in an intensified and shifted energy spectrum. The comparison is further supported by the spectral slope analysis, which consistently shows the two-scale spectrum surpassing PM at each specified wind speed, with the difference becoming more prominent as wind speed increases. In essence, the two-scale formulation results in a rougher and more complex ROM surface compared to PM at these wind speeds. This leads to greater ocean wave variance and roughness fluctuations, making it well-suited for ROM surface modeling and roughness pattern interpretations in remote sensing applications [94], [140]. Nonetheless, despite the two-scale WFS outperforming the PM model, Elfouhaily's

spectrum has a limitation in that it does not account for the directional distribution of significant wave heights based on wind speeds, known as angular spreading. This constraint hinders the accurate representation of fine details in significant wave patterns, especially regarding WFS skewing. The omission of directional spreading may overestimate flow velocities and wave heights, a critical factor that should not be overlooked [3]. To address this limitation, directional WFS formulations incorporating angular spreading functions are developed, as discussed in the subsequent section.

III. DIRECTIONAL TWO-SCALEWFS CONCEPT AND APPROACHES

Under steady sea state conditions with wind forcing, ocean waves generated by the wind propagate in the direction of the wind vector, with field measurements indicating that the spectral width is narrowest near the peak frequency and increases towards higher and lower frequency components [94], [96], [104], [105], [111]. This spectral distribution pattern is influenced by various physical processes, including wind-induced energy flux, energy dissipation, and nonlinear interactions, with their relative contributions varying at different stages of wave development. Therefore, examining the effects of wave components concerning sea state and gaining a comprehensive understanding of the physical mechanism of wind wave generation and distribution under these conditions can improve our ability to estimate ROM structural interactions and the behavior of wave patterns. As an approach, a relative algebraic formulation of the two-scale WFS under constant sea state conditions is considered. This formulation aims to replicate the directional characteristics of ROM interactions through the utilization of angular spreading functions, hereinafter referred to as directional two-scale WFS [74], [96], [103]. The directional formulation incorporates diverse empirical metrics to achieve satisfactory agreement in both hydrodynamic and energy scatterings across a broad frequency range, spanning both above and below the peak frequency [99], [104]. Nevertheless, it is crucial to recognize that while spreading functions effectively represent the directional distribution under varying sea state conditions, they can significantly smear the essential attributes of a wavefield distribution when wind and waves interact concurrently [96], [97], [103], [104]. As a result, there is a discernible need for a more realistic synthesis of directional WFS that establishes a correlation between the two-scale WFS and the angular spreading occurring within the fetch, particularly in relation to ROM surface roughness under varying sea states. This section, therefore, focuses on the formulation of directional WFS and angular spreading functions, accompanied by a series of well-established spreading functions intended for ROM numerical modeling.

A. ANGULAR SPREADING FUNCITON CONCEPT

By definition, the elevation spectrum can be mathematically defined as the Fourier transformation of the autocovariance function of surface displacements as [30], [42], [109]:

$$\Psi(k)= \mathrm{FT}\left\{\langle \eta\left(r_0\right)\eta\left(r_0+r\right)\rangle\right\} \tag{17}$$

where, FT is the Fourier transform operator, angle bracket denotes the ensemble average operator, η represents the surface elevation with zero mean, and r denotes the horizontal lag over the fetch. To account for the spatial variability of the spectrum, it is normalized as:

$$\begin{aligned}\sigma_\eta^2 = \left\langle \eta^2 \right\rangle &= \int_{-\infty}^{+\infty}\int_{-\infty}^{+\infty} \Psi\left(k_x, k_y\right) dk_x\, dk_y \\ &= \int_0^{\infty} \Psi\left(k,\varphi\right) k\, dkd\varphi = \int_0^{\infty} S(k)dk\end{aligned} \tag{18}$$

where, σ_η is the standard deviation of surface elevations, and $\Psi\left(k_x, k_y\right)$ and $\Psi\left(k,\varphi\right)$ are directional spectra in Cartesian and polar coordinates, with the wind assumed to be blowing in the positive x direction, referred to as downwind. Therefore, the omnidirectional spectrum of $S\left(k\right)$ is expressed as:

$$S\left(k\right) = \int_{-\pi}^{+\pi} \Psi\left(k,\varphi\right) k\, d\varphi \tag{19}$$

In order to separate the unidirectional dependence of the vector spectrum from the angular spread, one can write [94]:

$$\Psi\left(k,\varphi\right) = \frac{1}{k} S\left(k\right)\Phi\left(k,\varphi\right) \tag{20}$$

where, φ represents the wave direction relative to the wind, and Φ denotes the spreading function as [18] and [131]. In other words, calculating the directional WFS $\Psi\left(k,\varphi\right)$ entails multiplying the omnidirectional spectrum $S\left(k\right)$ by an angular spreading function $\Phi\left(k,\varphi\right)$, which can take different forms. Yet, a universally accepted formula for the spreading function is absent due to idealization and site-specific considerations, necessitating expert judgment for their application.

B. SERIES OF SPREADING FUNCTIONS FORMULATION

This section discusses various recognized spreading functions, all emphasizing directionality. Analyzing these functions allows for a reliable assessment of the directional characteristics of the two-scale WFS under sea state conditions, aiding in understanding the impact of angular spreading on ROM roughness.

1) COSINE TYPE

The earliest angular spreading function, known as the cosine-squared type, was utilized in the following form [145]:

$$\Phi\left(\varphi\right) = \begin{cases} \dfrac{2}{\pi}\cos^2\left(\varphi\right), & \text{for } |\varphi| \le \dfrac{\pi}{2} \\ 0, & \text{otherwise} \end{cases} \tag{21}$$

As the cosine-squared function remains independent of frequency and wind speed, researchers have adjusted exponent values and coefficients to modify directional spreading, including variations such as the cosine-fourth function, while ensuring adherence to the following condition:

$$\int_{-\frac{\pi}{2}}^{\frac{\pi}{2}} \Phi\left(\varphi\right) d\varphi = 1 \tag{22}$$

Later, a generalized form of the cosine-squared distribution, known as the cosine k-power distribution, was developed to offer a broader range of directionality as [145]:

$$\Phi(\varphi) = \begin{cases} \dfrac{\Gamma(k+1)}{2^k \Gamma^2\left(\frac{k+1}{2}\right)} \cos^k(\varphi), & \text{for } |\varphi| \le \dfrac{\pi}{2} \\ 0, & \text{otherwise} \end{cases} \tag{23}$$

where, Γ is the Gamma distribution function. Both the cosine-squared and cosine k-power functions, originally used for the half plane of $|\varphi| \le \pi/2$ to represent waves, encounter limitations in field experiments where wave components can extend beyond this range, thus limiting their applicability.

2) HALF-COSINE 2s-POWER TYPE

To cover the entire direction range of $0 \le \varphi \le 2\pi$, the half cosine $2s$-power function $\Phi(f, \varphi)$ was introduced, facilitating estimation of the angular extent of energy distribution within each frequency band, as follows [145]:

$$\Phi(f, \varphi) = N(s) \cos^{2s}\left(\frac{\varphi - \varphi_0}{2}\right) \tag{24}$$

$$N(s) = \frac{2^{2s}}{2\pi} \frac{\Gamma^2(s+1)}{\Gamma(2s+1)} = \frac{1}{2\sqrt{\pi}} \frac{\Gamma(s+1)}{\Gamma(s+0.5)} \tag{25}$$

where, f represents the wave frequency, s is the spreading parameter, and $N(s)$ is a normalizing function that ensures the condition of:

$$\int \Phi(f, \varphi)\, d\varphi = 1 \tag{26}$$

The spreading parameter regulates directional spreading around the mean wave direction and is derived from buoy measurements, involving Fourier coefficient calculations. The half cosine $2s$-power function identifies the principal direction for each frequency band, with narrower directional spread as the power of the cosine function increases.

3) PARAMETERIZED HALF COSINE 2s-POWER TYPES

To refine the half cosine $2s$-power spreading function, additional parameters have been introduced [109], [137]. For instance, Mitsuyasu et al. suggested determining the maximum spreading parameter associated with the peak frequency of the wave spectrum based on the non-dimensional wave age parameter, defined as the ratio of wave phase speed to wind speed, as follows [145]:

$$\begin{aligned} s_p &= 11.5\Omega^{-2.5} = 11.5\left(U_{10}/c_p\right)^{-2.5} \\ &= 11.5\left(2\pi f_p U_{10}/g\right)^{-2.5}, \text{ for } 0.7 \le \Omega \le 1.2 \end{aligned} \tag{27}$$

where, c_p denotes the phase speed at the peak frequency. They also extended their estimation and proposed an empirical formulation describing directional spreading variation with respect to spreading parameter as [33]:

$$\frac{s}{s_p} = \left(\frac{f}{f_p}\right)^{\mu} \tag{28}$$

where s_p represents the spreading exponent at the peak of the spectrum, denoted as f_p, while:

$$\mu = \begin{cases} -2.5, & \text{for } f \le f_p \\ 5, & \text{for } f > f_p \end{cases} \tag{29}$$

Later, investigations explored directional spreading under conditions of waves generated with veering wind, along with contributions from swells. Initially adopting the same parametrization, as reported by Hasselmann et al. [110], [145], they later proposed a new formulation upon observing no significant dependence on wave age. In their formulation, they found that the maximum spread remained constant, its value contingent on whether f was smaller or larger than peak frequency f_p, as stated below [146]:

$$\begin{cases} s_p = 9.77 \pm 0.43 \\ \mu = -(2.33 \pm 0.06) - (1.45 \pm 0.45)(\Omega - 1.17) \end{cases}, \text{ for } f > f_p \tag{30}$$

$$\begin{cases} s_p = 6.97 \pm 0.83 \\ \mu = 4.06 \pm 0.22 \end{cases}, \text{ for } f \le f_p \tag{31}$$

The values of s_p differ notably from Mitsuyasu's formulation, particularly at high frequencies influenced by wind velocity.

4) HYPERBOLIC SECANT-SQUARED TYPE

Due to incomplete experimental knowledge and the necessity to establish correlations between the spreading parameter and fundamental measurable wave parameters, Donelan et al. systematically measured directional spread spectrum values using a buoy array, proposing a hyperbolic secant-squared function instead of the half-cosine power type as [146]:

$$\Phi(f, \varphi) = \frac{1}{2} s \operatorname{sech}^2 s[\varphi - \varphi_0] \tag{32}$$

where, in the field data with $0.83 \le \Omega \le 4.6$, the spreading parameter s and the mean wave direction exhibit variations with respect to frequency as follows:

$$s = \begin{cases} 2.61\left(f/f_p\right)^{1.3}, \text{ for } 0.56 \le f/f_p \le 0.95 \\ 2.28\left(f/f_p\right)^{-1.3}, \text{ for } 0.95 < f/f_p < 1.6 \\ 10^{\left\{-0.4+0.83\exp\left[-0.56\ln\left(f/f_p\right)^2\right]\right\}}, \text{ for others } f/f_p \end{cases} \tag{33}$$

However, when $f/f_p = 0.95$, s= s_p indicates that the directional spreading is narrowest at the peak frequency and widens both above and below it. Nevertheless, this model does not incorporate a parameter to capture wave growth.

5) COMPOSITE STRUCTURED TYPE

Spreading functions must exhibit centrosymmetric properties because the directional spectrum is the Fourier transform of the bidimensional covariance of real and even surface displacement [49], [94]. This means that the Fourier series

expansion of the spreading function consists only of even harmonics, as follows:

$$\Phi(k,\varphi) = \frac{1}{2\pi}\left[1 + \sum_{n=1}^{\infty} a_{2n}\cos(2n\varphi)\right] \tag{34}$$

To ensure the centrosymmetric properties, an additional parameter, Δ, representing the downwind-crosswind ratio, is introduced. This ratio assists in deriving the second harmonic when truncating the Fourier series expansion of the angular function, as below:

$$\Phi(k,\varphi) = \frac{1}{2\pi}\left[1 + \Delta(k)\cos(2\varphi)\right] \tag{35}$$

$$\Delta(k) = \frac{\Phi(k,0) - \Phi\left(k,\frac{\pi}{2}\right)}{\Phi(k,0) + \Phi\left(k,\frac{\pi}{2}\right)} \tag{36}$$

where, Δserves as the coefficient for the second harmonic, which decreases as the wavenumber increases. To address interactions between independent long and short waves, it is assumed that long-waves are aligned with the mean wind direction under steady conditions, governed by the wavenumber factor $k_p/p \approx \left(c/c_p\right)^2$ [94]. Considering the natural involvement of the hyperbolic tangent function from the cosine function in (34) and its subsequent derivation in (36), alongside the inclusion of the phase speed ratio, a composite spreading function is formulated as follows:

$$\Delta(k) = \tanh\left\{a_0 + a_p\left(c/c_p\right)^{2.5} + a_m\left(c_m/c\right)^{2.5}\right\} \tag{37}$$

where, the constants $a_0 = 1.4\times10^{-2}$ and $c_m = 0.23$ are fixed values, and a_p and a_m are functions of U_{10}/c_p and U/c_m, as mentioned earlier. Worth noting that the Δ ratio in (36) exhibits a tangential form with a monotonically decreasing behavior, whereas (37) satisfactorily overcomes these limitations [94].

IV. NUMERICALROM MODELING ROUTINES

Modeling the surface roughness of the highly dynamic structure of ROM, considering sea state, is vital for addressing ocean remote sensing challenges such as momentum exchange, energy balance, electromagnetic interactions, and texture interpretation. The surface of the ROM, on the other hand, is characterized by stochastic scattering properties due to nondeterministic, time-dependent hydrodynamic interactions that evolve with sea states, emphasizing the importance of adopting a two-fold approach for accurate roughness modeling. The first aspect of this approach involves implementing a numerical routine to calculate the scattering of ocean waves across various temporal and spatial scales using the WFS scattering formulation. The second aspect entails incorporating the angular distribution of time-dependent wind-waves, considering various spreading functions under varying sea states, to account for the directional characteristics of the model. To implement such an approach, it is important to recognize the limitations of commonly accepted roughness modeling criteria, such as root-mean-square, maximum height, and skewness, which fail to capture the intricate and time-varying features of ROM across different length scales due to their scale-dependency. Therefore, it becomes imperative to adopt a feature-based method that transcends the constraints of a single or limited length scales. In this context, incorporating WFS enables the dynamic characterization of wind-wave generation across various wavelength scales, enhancing the precision in depicting the directional aspects exhibited by the two-scale formulation. This process involves calculating the elevation information age, indicating the height from the average plane, by superimposing short-wave and long-wave curvature spectrums that incorporate diverse wavenumbers and intensities derived from directional WFS formulation in a wave number scattering coordinate. This results in a complex dataset that adeptly portrays the intricate variations of ROM roughness features across distinct wavelength scales. Subsequently, the obtained dataset undergoes Fourier transformation, converting the surface data from the lateral wavenumber scattering coordinate system into a function of wave vector frequency.

In order to initiate the ROM modeling and characterize the wind-wave interactions, it is necessary to establish the scattering coordinate system, which is represented by a Cartesian system. This coordinate system features the XY plane that corresponds to the fetch with dimensions $L\times W$, while the Z-axis is oriented upwards, perpendicular to the mean plane at $z = 0$. The height, denoted by $Z(x,y)$, represents the surface elevation in meters at a given spatial location (x,y). Under specified sea state, characterized by the wind speed U and direction φ as depicted in Fig. 5, a boundary condition is adopted to ensure consistency between surface height and bidirectional spectral distribution. This enables the transformation of the directional WFS $\Psi(k,\varphi)$ into a Cartesian coordinate system, denoted as$\Psi\left(k_x,k_y\right)$, thereby making it feasible to extract elevation variance information in physical quantities through superimposition across all wavenumbers. To provide additional clarity to the coordinate system, it is specified that the X-direction represent the downwind direction, and in this context k_x corresponds to wave samples propagating in that specific direction. Likewise, the Y-direction corresponds to the crosswind direction, with k_y indicating the crosswind samples in that specific direction. Accordingly, in the context of a deep-water condition governed by the gravity wave dispersion relationship$\omega = \sqrt{gk}$, the magnitude and direction of the spectrum, represented by k and φ respectively, are related to the Cartesian coordinate samples k_x and k_y as follows:

$$k = \sqrt{k_x^2 + k_y^2} \tag{38}$$

$$k_x = k\cos\varphi \tag{39}$$

$$k_y = k\sin\varphi \tag{40}$$

where, the associated samples are uniformly distributed at intervals ofΔ, and the spacing can be determined as:

$$\Delta_x = \left\{-\frac{N_x}{2}+1, -\frac{N_x}{2}+2, \cdots, \frac{N_x}{2}-1, \frac{N_x}{2}\right\}\frac{1}{L} \tag{41}$$

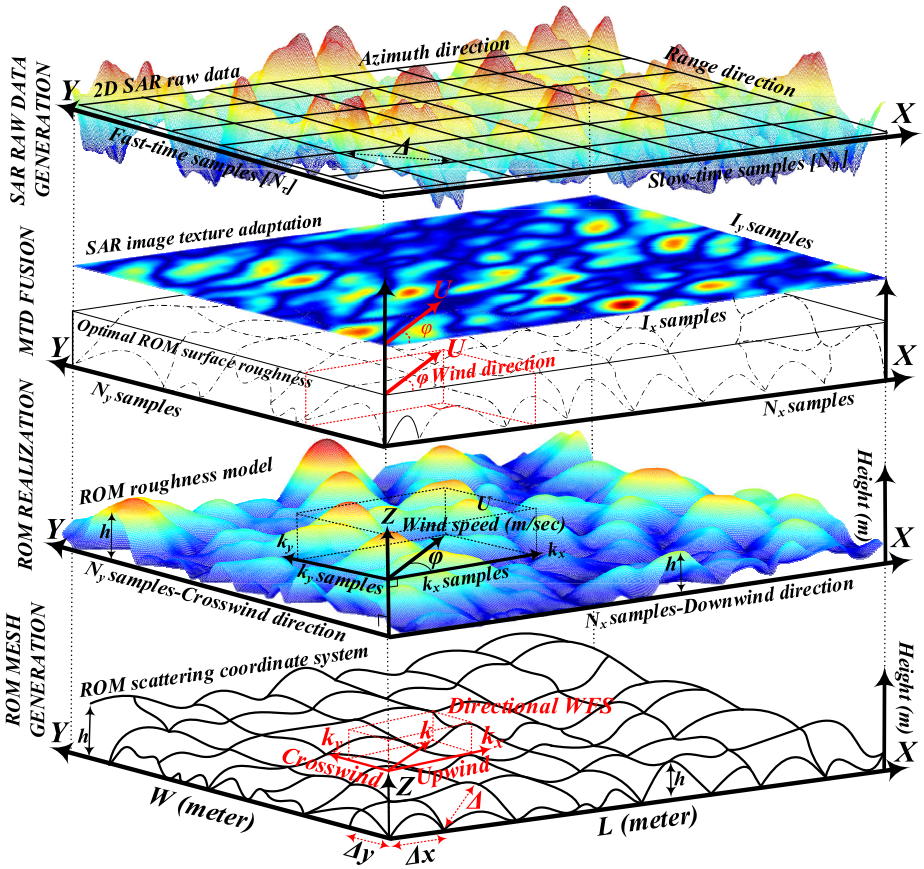

FIGURE 5. ROM boundary conditions, surface roughness pattern reconstruction, MTD features fusion and SAR dataset configuration.

$$\Delta_y = \left\{ -\frac{N_y}{2}+1, -\frac{N_y}{2}+2, \cdots, \frac{N_y}{2}-1, \frac{N_y}{2} \right\} \frac{1}{W} \tag{42}$$

where, N_x and N_y represent the number of samples at which the spectrum will be calculated.

Worth noting that the conversion of $\Psi(k,\varphi)$ to $\Psi(k_x,k_y)$ involves the cancellation of the k factor in (18) by $1/k$ in (20) through the Jacobian calculation, ensuring that the directional WFS having the same unit of $m^2 \Big/ (rad/m)^2$. Moreover, $\Psi(+k) \neq \Psi(-k)$, due to the tendency of more energy propagating upward at a given frequency. This underscores the significant role of the directionality effect, resulting in a higher concentration of energy variance in waves propagating upward along the φ direction compared to other directions. Incorporating these insights enables the establishment of ROM directional spectral scattering characterization, facilitating the implementation of two-scale WFS and subsequent ROM roughness modeling. It is crucial to note that directional WFS encompasses essential statistical properties related to surface scattering, with spectrum moments playing a pivotal role in determining quantities like mean surface roughness. Therefore, when implementing the ROM roughness modeling routine, careful selection of fetch boundary conditions aligning with theoretical and experimental principles is essential. This ensures the generation of a dataset $Z(x,y)$, with N_x and N_y samples, capturing uncorrelated structural information pertaining to the dominant sea state in the fetch with dimensions of L and W, obtained at regular spatial intervals Δx and Δy. Note that the number of samples, determined by the spatial intervals, directly impacts model resolution. Thus, selecting ROM resolution involves a trade-off between accuracy and computational efficiency, with finer resolutions increasing sample numbers and computational complexity, while coarser resolutions reduce the number of samples and computational burden.

Taking all of that into considerations, as shown in Fig. 6, the spectral components of the two-scale WFS are generated based on the defined Cartesian system and the specified boundary conditions. These components comprise the high-frequency B_h and the low-frequency curvature spectrums B_l, frame formatted to match the scattering dataset attributes and sea state. Following this, the omnidirectional two-scale WFS $S(k)$ is obtained by adding these two curvature spectrums. Once the composite WFS is formed, the selected directional spreading function $\Phi(k,\varphi)$, which is highly influenced by wind direction, is formulated and adjusted to align with the coordinate system. To ensure efficient spreading function implementation, parallel processing is utilized for accelerated computation. In the subsequent step, the directional two-scale WFS $\Psi(k,\varphi)$ is constructed through spectral multiplication. It is important to note that each sea state condition, along with its corresponding spreading function, exhibits a unique

variance spectrum resembling a random distribution, representing directional scatterings. Hence, for generating the ROM surface model, a set of discrete Gaussian samples, randomized in nature, is defined and aligned with the directional two-scale WFS. These samples intricately modify the wave height information by introducing random amplitudes and phases, thereby facilitating the generation of the roughness samples based on the square root of the spectrum of different frequency components under varying sea state conditions. During modeling, the inherent Gaussian variability embedded in these spectra is averaged out, retaining only the variance spectrum. To maintain surface texture consistency, interpolation techniques are utilized, ensuring a smooth transition in elevation information during sample generation.

Finally, the inverse 2D FFT is computed, resulting in a complex dataset representing the surface elevation, with the real part corresponds to physical wave heights. A detailed illustration of the entire numerical ROM modeling routine is presented in Fig 6. It is worth noting that implementing the two-scale directional WFS function requires careful data size matching during modeling, involving surface meshgrid generation with desired resolution and consideration of directionality effects of spreading functions relative to sea state, especially wind direction. Consequently, the conventional autocorrelation approach proves inadequate for accurately modeling ROM surfaces. Instead, employing a filtering approach with Gaussian information distribution followed by a 2D FFT algorithm proves more suitable for such composite modeling.

Considering the objective of this manuscript, which is to investigate the directional scattering properties of wind waves under varying sea states, a comprehensive analysis will be conducted on the reconstructed ROM models. This entails investigating composite directional ocean wave spectra derived by multiplying spreading functions with the formulated two-scale WFS. Through exploring these spectra and their corresponding roughness models, this survey aims to enhance understanding of estimating ROM roughness profile fluctuations and their impact on electromagnetic interactions. Detailed discussions on these aspects will follow in subsequent sections.

V. ROM SURFACE ROUGHNESS MODELING AND SCATTERING DISTRIBUTION MODE ANALYSIS

To effectively investigate the ROM modeling routine, it is crucial to consider the contribution of spreading functions and their scattering effects on directional distribution, given their significant influence on the wave pattern. In this context, various spreading functions, including the half-cosine 2s, parameterized half-cosine types such as the Mitsuyasu and Hasselmann formulations, hyperbolic secant-squared, and composite structured type, are examined under identical boundary conditions with a moderate wind speed of 8m/sec and varying wind directions [147]. The wind direction is incrementally varied in steps of 18 degrees, ranging from 0 degrees in the downwind direction to 90 degrees in the

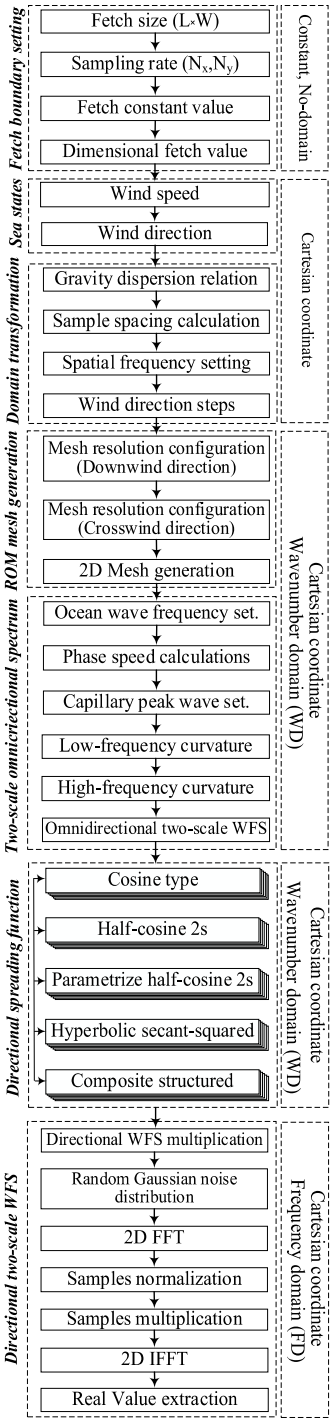

FIGURE 6. ROM surface roughness modeling routines.

crosswind direction. These considerations are incorporated into the ROM modeling routine depicted in Fig. 6, resulting in the generation of ROM roughness models presented in Fig. 7. As shown in Figs. 7(a) to 7(f), the models display distinct wave patterns and orientations consistently aligned with the wind direction. For instance, Fig. 7(a) with a wind direction of 0 degrees exhibits random ocean waves predominantly oriented in the downwind direction, while Fig. 7(f) with a wind direction of 90 degrees shows waves mainly oriented

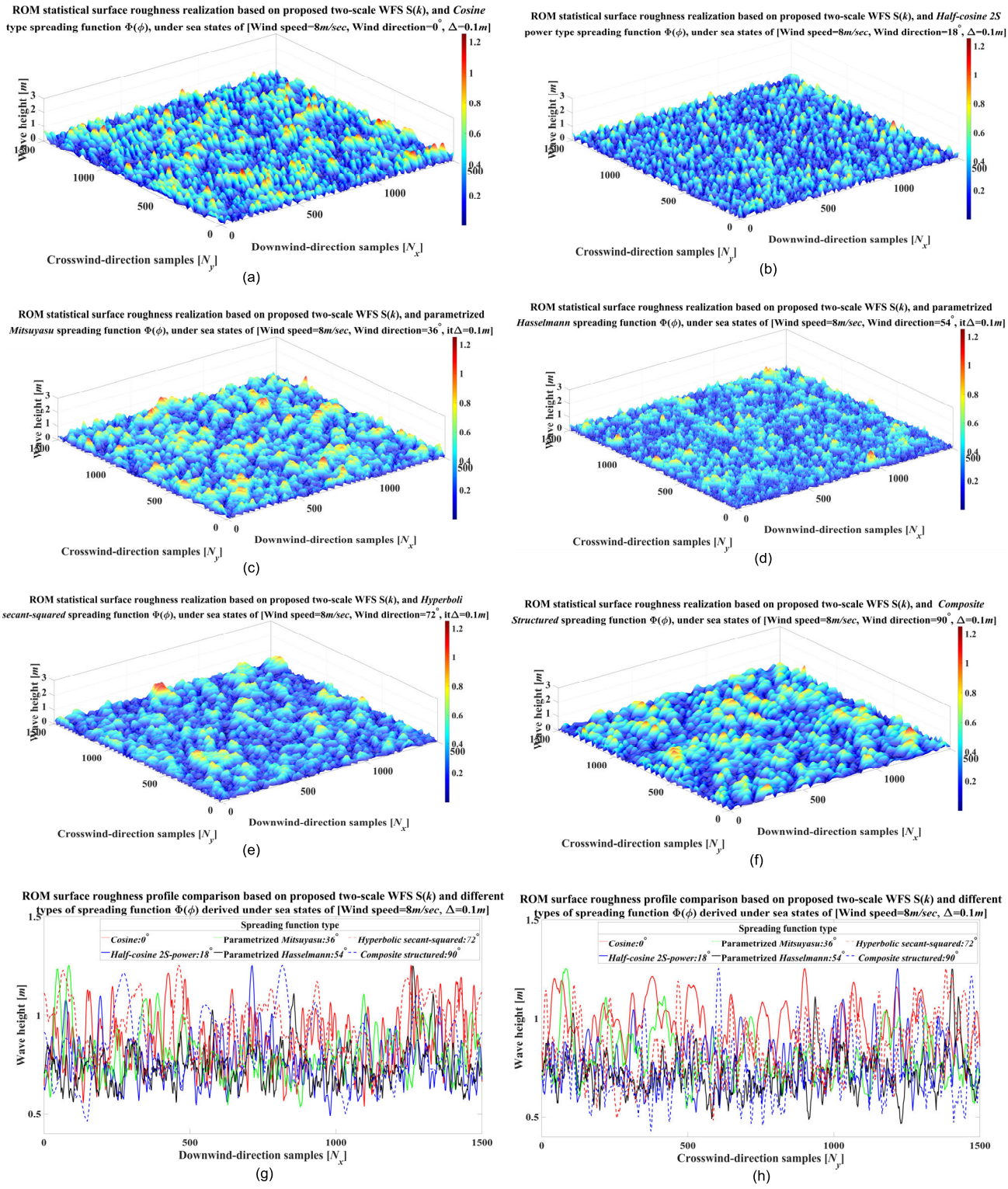

FIGURE 7. ROM surface roughness modeling results based on fixed wind speed of 8 m/s and varying wind directions using different spreading functions (a) Cosine, (b) Half-cosine 2 s-power, (c) Parameterized half-cosine Mitsuyasu, (d) Parameterized half-cosine Hasselmann, (e) Hyperbolic secant-squared, (f) Composite structured, (g) Downwind direction roughness profile presentation of (a) to (f), (h) Crosswind direction roughness profile presentation of (a) to (f).

in the crosswind direction, perpendicular to the downwind direction. This consistent trend of roughness pattern can be observed for other wind wave directions at 18-degree steps, as illustrated in Figs. 7(b) to 7(e).

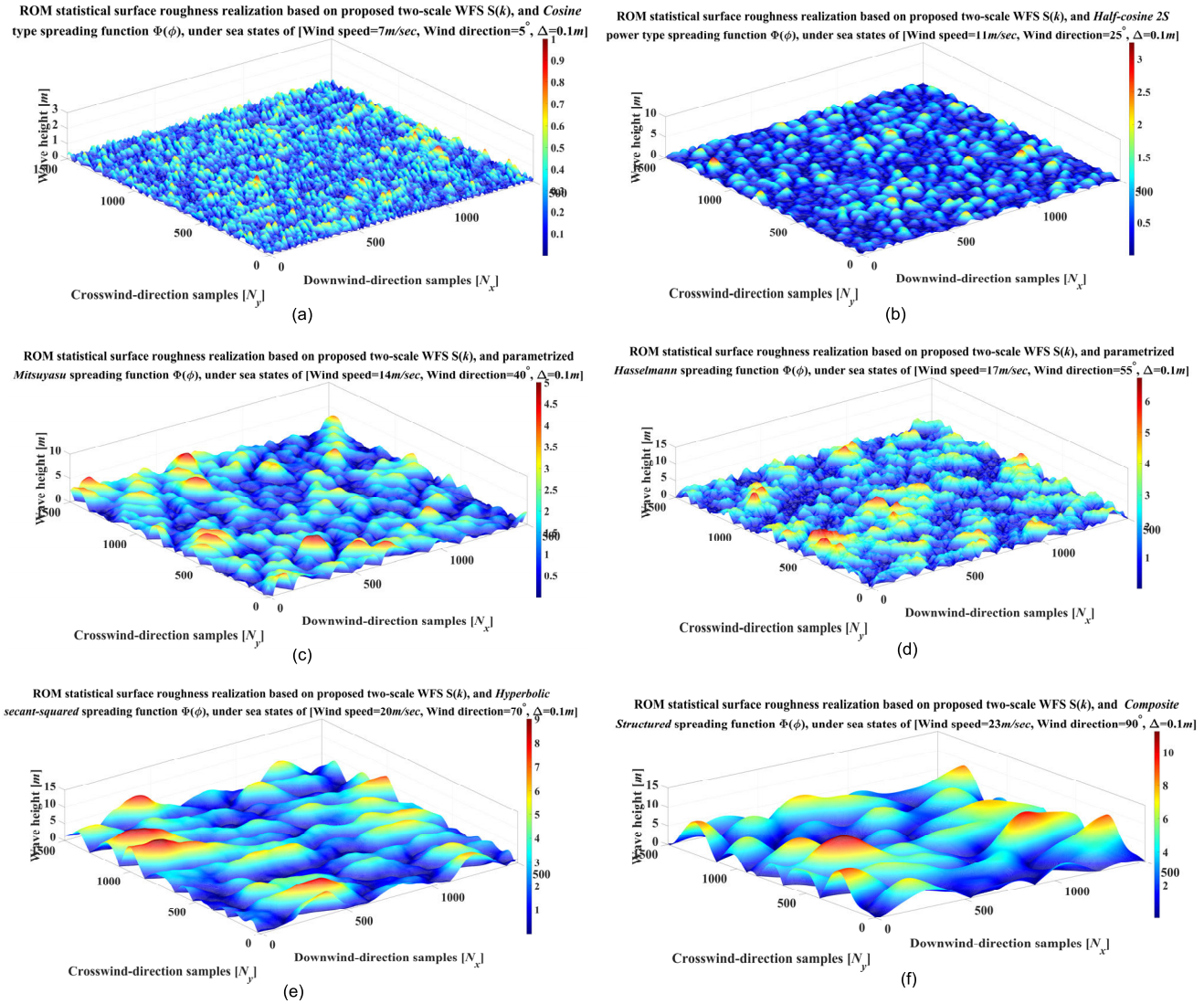

FIGURE 8. ROM surface roughness modeling results based on varying wind speeds and directions using different spreading functions (a) Cosine, (b) Half-cosine 2 *s*-power, (c) Parameterized halfcosine Mitsuyasu, (d) Parameterized half-cosine Hasselman, (e) Hyperbolic secant-squared (f) Composite structured.

The results further reveal that regardless of the spreading functions and wind directions used, each ROM model consistently display a maximum wave height of nearly 1.25 *m* at wind speed of 8 *m/sec*. This suggests that wind direction influences the orientation of the ROM roughness pattern, redistributing composite spectral components while maintaining a consistent maximum height, despite ocean wave height variations. For additional insight, Figs. 7(g) and 7(h) depict detailed representations of the maximum roughness profile within a specified fetch of 150 *m* in both the downwind and crosswind directions for the models shown in Figs. 7(a) to 7(f). The results also highlight that the wave height profile includes ripples and random roughness fluctuations in both directions, maintaining the maximum wave height consistently irrespective of sea states and spreading functions. Specifically, the roughness profile shows rapid variations in wave height at lower elevations near the mean zero level, followed by smoother transitions to higher peaks. These behaviors suggest the presence of inherent fractal properties in wave patterns, generating roughness fluctuations across various scales. The composite structure of the two-scale WFS and spreading functions, influenced by the sea state, significantly contribute to these fractal properties observed throughout the entire fetch in both directions.

To gain a detailed understating of ROM roughness variations, especially in synthesizing wave patterns under dynamic sea states, it is crucial to analyze the wave height profile using directional two-scale WFS with varying wind speeds and directions [65]. To this end, a detailed assessment is conducted to evaluate the impact of spreading functions on ROM roughness patterns, considering their response to sea states. This synthesis involves assigning different spreading functions to different sea states, facilitating a thorough evaluation of the directional WFS. In doing so, the sea states

are categorized into seven major physical states, ranging from smooth sea states with wind speeds below 3.5 m/s to very-high states approaching 24 m/s, as listed in Table 1 [147]. It should be noted that smooth and slight sea states, characterized by wind speeds below 7 m/s, are excluded from the assessments due to their relatively small-scale heights of less than 1 m compared to the other five major states. The assessment results, as presented in Fig. 8 and summarized in Table 1, highlighting the significant influence of sea states, including wind speeds, wind directions, and spreading function types, on both the maximum wave height and the roughness profile. Comparing Fig. 8 to Fig. 7 reveals the noticeable impact of changes in sea states on maximum wave heights and overall wave patterns. Increased wind speed correlates with higher wave heights, while variations in wind direction or spreading function induce changes in the roughness pattern, aligning it with the wind direction. This highlights the dynamic characteristics of ROM surface and underscores the inherent fractal properties shaped by directional WFS. To delve deeper into these dynamic characteristics and fractal fluctuations, a comprehensive analysis of ROM modeling investigates the influence of directional WFS formulation and its scattering characteristics in response to dynamic sea states. This analysis includes two additional evaluation scenarios. Firstly, the maximum wave height is determined for each categorized sea state using randomly assigned spreading functions, as outlined in Table 1. Secondly, the analysis focuses on the scattering distribution mode, examining the scattering pattern and scattering orientations of directional WFS concerning the assigned spreading function types and their response to diverse sea states, as depicted in Figs. 9 and 10

Referring to Table 1, a correlation emerges between the progression of sea states and the corresponding maximum wave height. Ocean wave heights increase progressively from approximately 1 m in moderate sea states with a wind speed of 7 m/s to over 12 m in very-high sea states with a wind speed of 24 m/s. This increase in maximum wave height coincides with a simultaneous rise in wave height fluctuations, consistent with trends observed in Figs. 2 and 4. To analyze the spectral scattering distribution mode of ROM, spectral scattering contours, referred to as scattering pattern, are simulated in Fig. 9. The contours illustrate directional scattering distribution of the formulated WFS influenced by the spreading function and input sea states. For standardized investigation of distribution mode, each specified directional WFS, characterized by its assigned spreading function, underwent evaluation under the same very-rough sea state conditions, featuring a wind speed of 12 m/s and a wind direction of 30 degrees. The findings of this evaluation reveal that each directional WFS exhibits a unique scattering distribution mode influenced by its assigned spreading function, leading to variations in both the scattering pattern and scattering orientation [97].

Notably, the scattering orientations depicted in Fig. 9 consistently align with the wind direction, emphasizing the

TABLE 1. ROM surface roughness profile evalaution based on sea state classification conditions.

Spreading Function	Sea state conditions		Maximum wave height [m]	ROM Physical state
	Wind speed [m/sec]	Wind direction [degree]		
Cosine type	7	5	0.99	Moderate
	8	10	1.25	Moderate
	9	15	1.49	Rough
Half cosine 2s-power type	10	20	2.50	Very-rough
	11	25	3.24	Very-rough
	12	30	3.99	Very-rough
Parameterized half-cosine, *Mitsuyasu*	13	35	4.49	High
	14	40	5.00	High
	15	45	5.50	High
Parameterized half cosine, *Hasselmann*	16	50	5.99	Very-high
	17	55	6.74	Very-high
	18	60	7.44	Very-high
Hyperbolic secant squared type	19	65	8.25	Very-high
	20	70	8.99	Very-high
	21	75	9.75	Very high
Composite structured type	22	80	10.5	Very-high
	23	85	11.24	Very-high
	24	90	12	Very-high

significant influence of wind direction on the orientation of the wave pattern. In other words, when considering the distribution of directional WFS and its impact on ROM surface roughness, both sea states, with a particular emphasis on wind direction, and the spreading function play crucial roles in shaping the scattering pattern and orientation of the roughness. These factors contribute to the distinct fractal features observed in ROM roughness profile, emphasizing the complex interplay between sea state, wind direction, and spreading function in determining the scattering distribution mode [97]. To further explore these intricate ROM directional WFS properties, Fig. 10 investigates the spectral distribution mode of the Mitsuyasu spreading function. The figure presents two sea state scenarios, one with a fixed wind speed and variable wind directions, and the other with variable wind speeds and directions. As depicted in Fig. 10, the scattering pattern remains largely consistent in both scenarios, while the scattering orientation consistently aligns with the specified wind direction, resulting in a distinct directional distribution. This indicates that the spectral distribution mode, particularly the scattering pattern, is determined by the directional WFS formulation, while the scattering orientation is influenced by the wind direction, and the intensity, represented by wave height, is influenced by the wind speed. In summary, achieving the ROM model requires formulating a directional WFS that aligns with spreading function multiplication and responds to dynamic sea states. This entails investigating wave scattering modes under varying wind speed and direction to determine both the wave scattering pattern and roughness orientations. To perform a detailed analysis of spectral scattering distribution, power spectral density (PSD) function modeling of directional WFS was conducted using the Mitsuyasu spreading function. The results are presented in Figs. 11 to 13, with Figs. 11(a) and 11(b) illustrating the unidirectional PSD function for both the downwind and crosswind directions under the high sea state conditions,

with a wind speed of 14 m/s and an average direction of 45 degrees.

As can be deduced, that the PSD components comprehensively occupied nearly the entire range of the spectral domain within their respective directions, with spectral interactions increasing as frequency rises. Comparing the bidirectional PSD function in Fig. 11(c), representing the entire fetch domain, to its unidirectional counterparts, the bidirectional model presents a unified and coherent peak in the low-frequency range. This major peak effectively fills the low-frequency spectral regions observed in Figs. 11(a) and 11 (b), indicating its ability to complement ocean WFS scattering characteristics and provide full spectral coverage. The distinct properties of the PSD functions stem from the formulation of directional WFS, influencing intricate spectral interactions and significantly the ROM's scattering distribution mode. In essence, the low-frequency components of the PSD represent the ROM's dominant roughness features, characterized by long waves with distinct structures. Conversely, the medium and high-frequency components capture the effects of the spreading function and the high-frequency curvature spectrum, shaping the ROM's roughness fluctuations [97]. It is noteworthy that both the unidirectional and bidirectional PSD functions exhibit symmetric scattering patterns around the origin, highlighting the importance of centrosymmetric spectral properties in the two-scale WFS formulation. These spectral properties extend beyond the specific sea state and Mitsuyasu spreading function mentioned, being applicable to other spreading functions under diverse sea states, albeit with potential variations in interaction behaviors and intensities. For instance, in Fig. 12, a PSD investigation is conducted on the Mitsuyasu spreading function under high sea state condition with a wind speed of 14 m/s and variable wind directions. The unidirectional PSD profiles in Figs. 12(a) and 12(b), along with the bidirectional profile in Fig. 12(c), exhibit similar spectral interaction behaviors as observed in Fig. 11. The bidirectional PSD function demonstrates a narrowing trend in the low-frequency region as the wind direction deviates from downwind to crosswind direction, indicating a more focused energy distribution in specific wave directions. Conversely, the unidirectional PSD function displays higher power at 0 and 90 degrees, corresponding to wind directions. This suggests that as the frequency increases, the unidirectional PSD function becomes stronger when the wind speed remains constant and wind direction varies, with maximum intensity observed in the downwind or crosswind direction. However, as the mean wind direction approaches the medium direction of 45 degree, the intensity of the unidirectional PSD function decreases, while the overall trend of spectral scattering and their interactions remains consistent [97], [115].

Remarkably, the behavior observed in bidirectional PSD function model can be attributed to the characteristics of the low-frequency components governed by directional WFS, particularly in the context of the two-scale WFS formulation. This narrowing trend and heightened spectral interactions in the low-frequency range, corresponding to the low-wavenumber curvature spectrum, underscore their resilience to changes in wind direction. These low-frequency components play a crucial role in shaping non-overlapping structures with higher consistency, resulting in the generation of major surface structures within the ROM surface. Conversely, the broader and weaker spectral interactions of the unidirectional PSD components in the medium to high-frequency range, corresponding to the high-wavenumber components of the two-scale WFS, play a pivotal role in forming overlapping fractal structures including ripples, turbulences, and fluctuations. These fine detailed structures are influenced by wind direction, ultimately result in the formation of highly-textured areas in the wave pattern. Figure. 13 depicts PSD profiles for high and very-high sea states using the Mitsuyasu spreading function, providing insight into how sea states influence directional WFS spectral interactions and ROM roughness patterns. The simulations cover wind speeds ranging from $13m/s$ to $17m/s$, with a constant wind direction of 45 degrees. Both unidirectional and bidirectional PSD profiles exhibit comparable spectral interaction patterns under varying wind speeds while maintaining a fixed direction, as seen in Fig. 12. However, discernible differences in magnitude suggest that changes in wind speed distinctly influence composite spectral interactions, apart from wind direction impacts.

Notably, increasing wind speed in the unidirectional profiles of Figs. 13(a) and 13(b) leads to more rapid and significant variations in spectral interactions associated with high-wavenumber components. This implies a higher occurrence of highly-textured areas at higher wind speeds, albeit with relatively weaker intensities at certain frequencies compared to those observed in Figs. 12. These areas arise from the interactions among gravity-capillary waves, involving wide-band ocean wave intermodulations and dispersion effects, as observed in the PSD profile with varying wind direction in Figs. 12(a) and 12(b) [37], [75]. Moreover, the spectral interaction behavior demonstrated in Fig. 13(c), influenced by low-wavenumber components representing long-wave structures affected by resonant modulation impacts and narrow-band filtering effects of fetch, signifies the formation of major texture entities within ROM surface. This structural pattern of wave behavior is notably influenced by sea state conditions, with wind speed being a significant factor [37], [94]. Analysis of Figs. 12(c), 13(c), and Table 1 data reveals a decreases in the magnitude of the bidirectional PSD profile with increasing wind speed. This decrease in power is attributed to the presence of larger wave heights, indicating greater consistency in the major structure of ROM roughness, characterized by non-overlapping structures generated by long-waves at higher wind speeds. On the contrary, an increase in wind direction results in the narrowing of the PSD function, particularly for low-wavenumber components, primarily influencing the scattering orientation of ocean waves rather than their intensity. These observations suggest that, despite the stochastic nature of two-scale

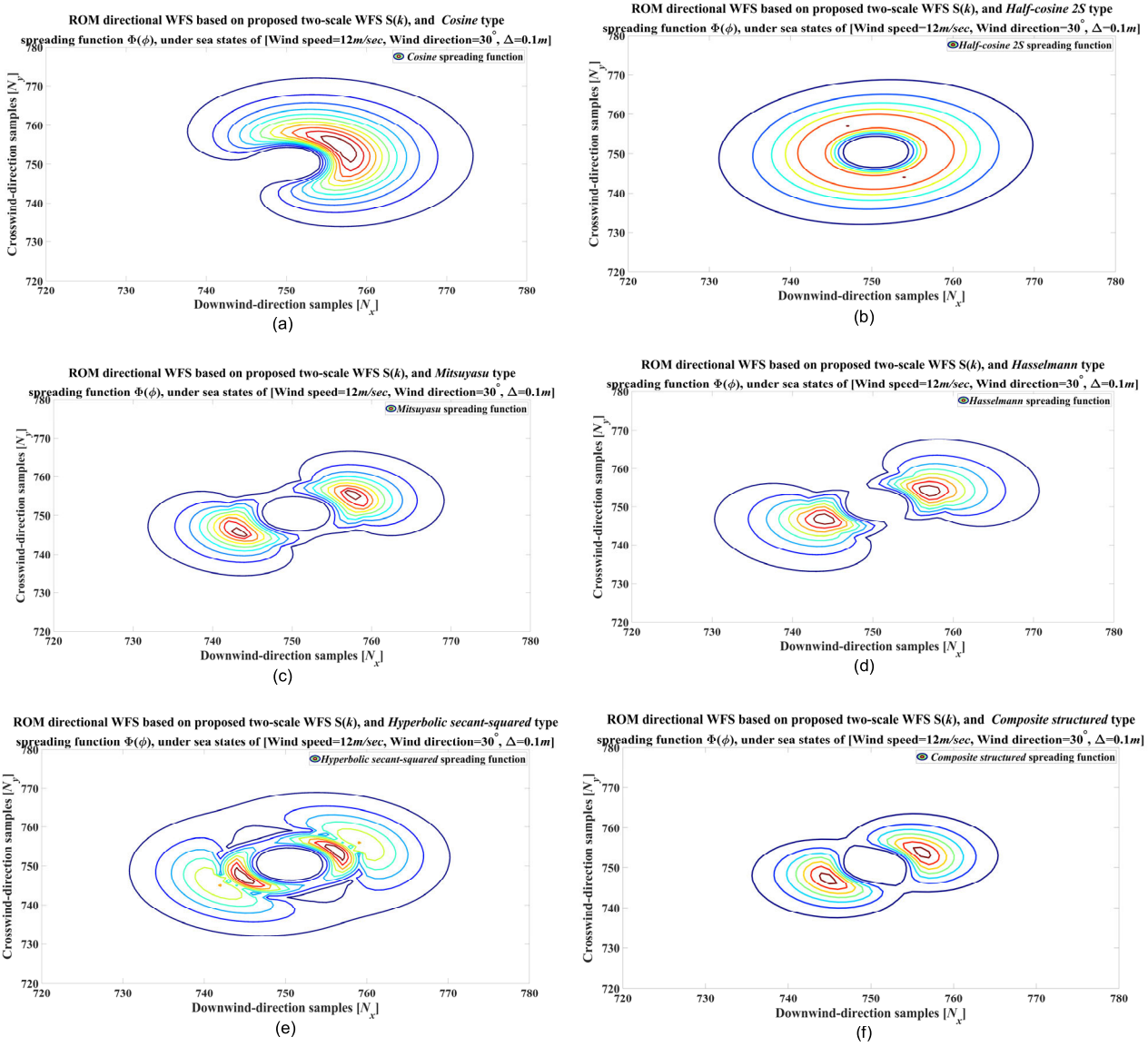

FIGURE 9. ROM directional WFS synthesis based on different spreading function under varying wind speeds and directions (a) Cosine, (b) Half-cosine -power, (c) Parameterized half-cosine Mitsuyasu, (d) Parameterized half-cosine Hasselmann, (e) Hyperbolic secant-squared, (f) composite structured.

WFS components and variations in PSD interactions, the proposed spectral formulation for achieving the ROM model remains applicable across diverse sea states with different spreading functions [97]. Put simply, the energy scattering contributions from the physical states, combined with the extent and dynamic interactions of the directional WFS, can be utilized to generate a distinctive fractal wave pattern with notable structural properties in the ROM, as intended.

Accordingly, a thorough investigation into the fractal surface roughness profiles of ROM has been conducted across four distinct categories of sea states, including moderate-rough, very-rogh, high, and very-high states. This analysis utilized directional WFS with different spreading functions, considering varying wind speeds and directions. The results, presented in Fig. 14., show case the maximum average ocean wave height for each sea state, represented by a sloid black line. The hatched area in the simulation results outlines the boundary of the roughness profile encompassing all individual ROM models. For instance, in Fig. 14(a), the solid black line represents the maximum average roughness profile in a moderate-rough sea state, with wind speeds ranging from 7 m/s to 9 m/s and wind directions from 0 to 90 degrees. The hatched area represents the roughness boundary where ROM models demonstrate variations in wave height values, providing insights into roughness fluctuations. As sea state levels progress from moderate to very-high, the roughness profile exhibits a wider boundary area and increased peak-to-peak sizes, consistent with earlier results. The shape of the hatched area is influenced by wind direction and the type of spreading function used, while its magnitudes is determined by wind speed.

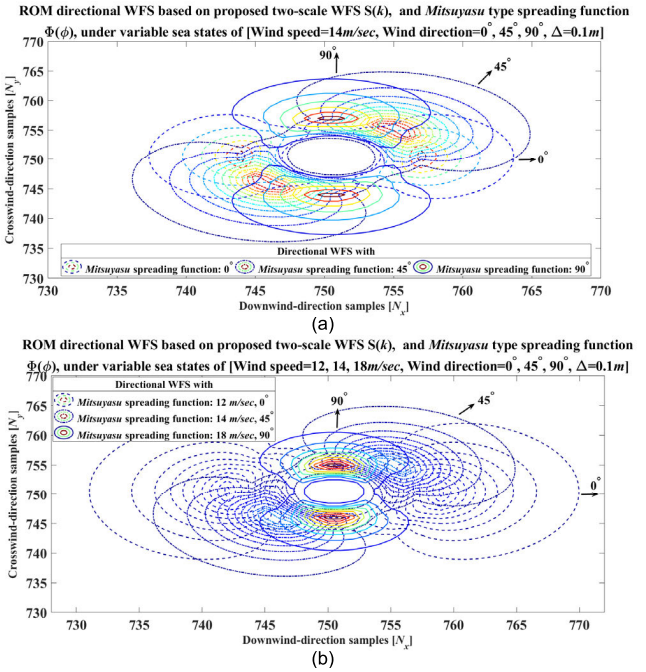

FIGURE 10. ROM directional WFS synthesis based on Mitsuyasu spreading function under (a) fixed wind speed and variable wind directions, (b) variable wind speeds and directions.

As wind speed and wave height increase, the roughness profile of the ROM undergoes a transition from small-scale waves with rapid height alterations, indicating highly-textured areas, to more uniform structures with enhanced consistency. Consequently, each ROM surface exhibits unique wave pattern characteristics influenced by sea states and the formulation of the directional WFS [74]. These versatile roughness fluctuations give rise to a wide range of surface structures, resulting in unpredictable variations in its electromagnetic interaction estimations, which poses challenges in accurately predicting backscattering properties [87]. To address this issue, the upcoming section will explore ROM electromagnetic interactions using a deep learning approach sensitive to roughness patterns in the transform domain, aiming to provide valuable insights and effective solutions.

VI. OPTIMAL ROM ROUGHNESS FRACTAL FEATURES FUSION AND SAR RAW DATA GENERATION

Microwave remote sensing is of utmost importance in the context of global ocean observations, with SAR imaging proving particularly adept in various tasks such as mapping ocean currents, identifying wave generation regions, estimating wave distribution and phase speed, assessing sea states, and inferring information about the intricate structures of ocean surface [91], [92]. However, when designing a SAR sensor, a trade-off must be made between radar spatial resolution and the complexity of the image formation algorithm (IFA) due to the time-varying ocean wave height variations [122]. These roughness fluctuations lead to random non-coherent backscattering in the received signal, causing dataset inconsistencies, resolutional anomalies,

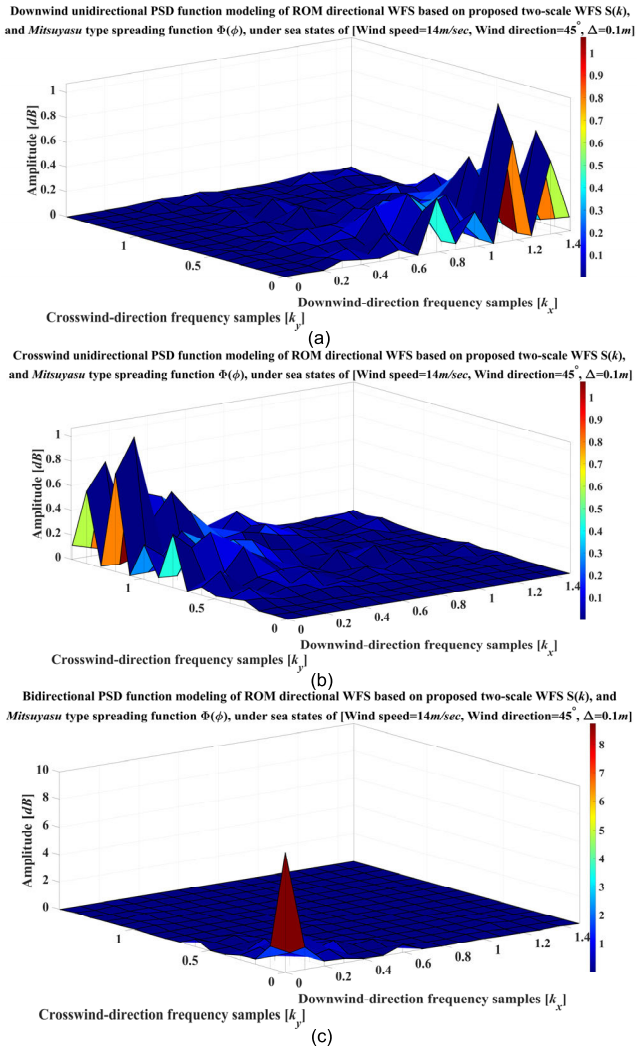

FIGURE 11. PSD function modeling of ROM directional WFS based on Mitsuyasu spreading function type under specified sea state condition in (a) Downwind-direction, (b) Crosswind-direction, (c) Bidirectional domain.

and potential misinterpretations of texture, posing challenges for real-time ocean observations [60], [148]. Hence, investigating the electromagnetic interaction between the SAR sensor and ROM roughness models is highly advantageous for extracting properties related to uncorrelated ocean surface backscattering and developing an effective IFA for interpreting ocean surface behaviors [59]. However, the directional distribution of the two-scale WFS introduces heuristic effects on ROM roughness, as the spreading function does not decisively determine the optimal formulation for providing surface structure details [65], [145]. Hence, from a SAR observation point of view, these nondeterministic and time-dependent roughness fluctuations can result in uncorrelated and non-coherent reflectivities [148], leading to degraded electromagnetic interactions and dephased echo with a diverse range of backscattering coefficients [149]. In other words, constraints imposed by the contributions of low and high-wavenumber spectral components to ROM roughness, influenced by various spreading functions and

sea states, limit SAR investigations into the backscattering properties of texture using reconstructed ROM models [147].

To address uncertainties in spreading function application and achieve an optimal ROM model for texture electromagnetic interaction investigations, a MTD fusion technique is proposed here [125], [126]. This method overcomes challenges of manual measurements and fusion rules by conducting joint measurements and fusion through a learning process [128], offering advantages over existing methods. To investigate the fusion results, referred to as the optimal roughness model, an inverse problem solution is applied to the fused roughness model for SAR raw data generation (RDG) [149]. In this context, the upcoming section will introduce the MTD fusion approach, employing a CNN, and then present the inverse equalized hybrid-domain algorithm for RDG, which effectively addresses the challenges of domain adaptability and spatial variations in the echoed spectrum. To the best of the author's knowledge, no research manuscripts have reported the generation of an optimal ROM roughness profile and investigation of its relevant texture electromagnetic interactions. To further validate the efficacy of the proposed MTD fusion and RDG, objective quality assessment technique are provided alongside simulations, demonstrating the method's efficacy.

A. ROM OPTIMAL ROUGHNESS MODEL GENERATION BASED ON DEEP LEARNING FUSION APPROACH

Various data fusion techniques have been developed, broadly classified into transform domain and spatial domain methods [124]. These approaches rely on two crucial processing steps, namely features extraction and coefficients mapping, to assess measurements by extracting detailed structural information from registered data and ensuring consistent scaled mapping of coefficients from segmented structures. These measurements are then compared using carefully adopted fusion rules to generate a fused map containing integrated information. However, in most existing fusion schemes, these two steps are designed separately and optimized manually, making it challenging to develop an optimal fusion rule that considers all necessary aspects of input data. This complexity is further heightened when fusing ROM models influenced by diverse WFS formulation under different sea states, resulting in different scattering distribution modes that modify the directional wave patterns, leading to multi-mode local structures with time-varying roughness patterns. In this context, the MTD fusion method, capable of merging decomposed coefficients to combine complementary structural information from multi-mode inputs, offers the potential for higher consistency in fusing ROM models compared to spatial-domain methods. However, it is important to consider that when dealing with surface roughness pattern, the design and optimization of ROM fusion schemes based on data decomposition have limitations, rendering them susceptible to roughness fluctuations, and textured area in particular. Moreover, the complexity is further compounded by the requirements for specific fusion rules for each ROM model,

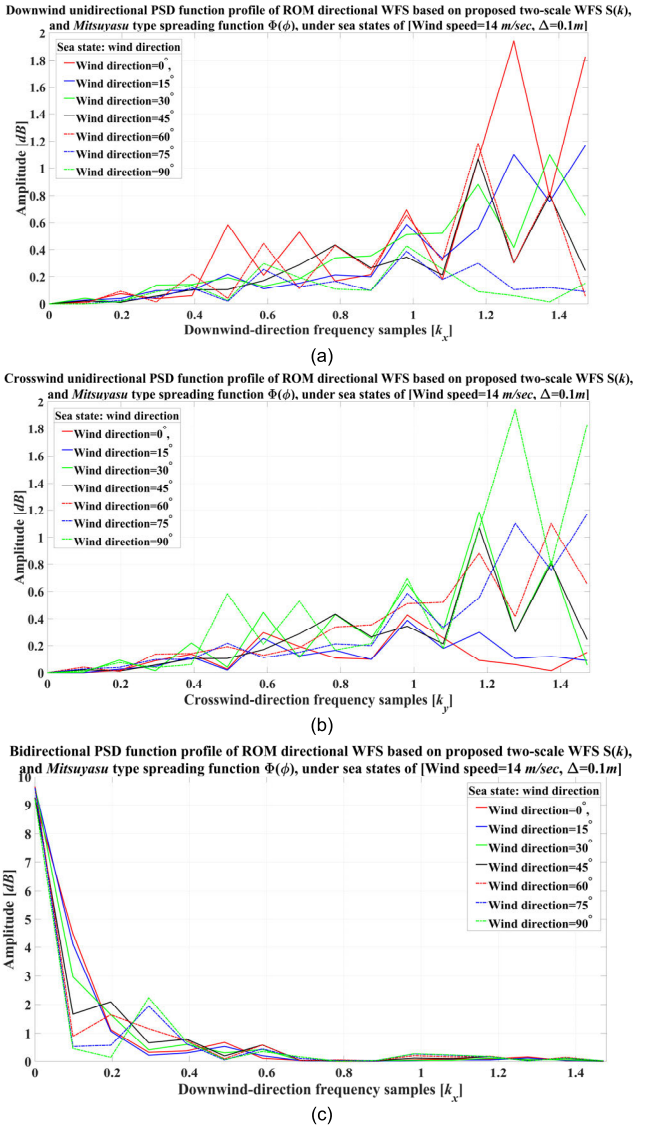

FIGURE 12. PSD function profile of ROM directional WFS based on fixed wind speed and varying wind directions using Mitsuyasu spreading function type in the (a) Downwind-direction, (b) Crosswinddirection, (c) Bidirectional.

given their varied roughness patterns resulting from diverse scattering distribution modes. This intricacy adds layers of complexity to the fusion scheme. In response, deep learning presents a novel solution for ROM roughness fusion. Leveraging its agile and adaptive non-linear capabilities, deep learning enables the MTD fusion scheme to adapt to various roughness pattern stemming from different directional WFS formulations. This adaptability facilitates enhanced roughness reconstruction and texture synthesis under multi-mode scattering conditions [150].

To this end, a deep learning fusion scheme based on CNN registration and Laplacian pyramid (LP) fusion using local gradient energy (LGE) strategy is proposed to fuse ROM models [125], [126], thereby enhancing the performance of the MTD fusion method. In this scheme, illustrated in Fig.15, two highly correlated ROM models derived under similar

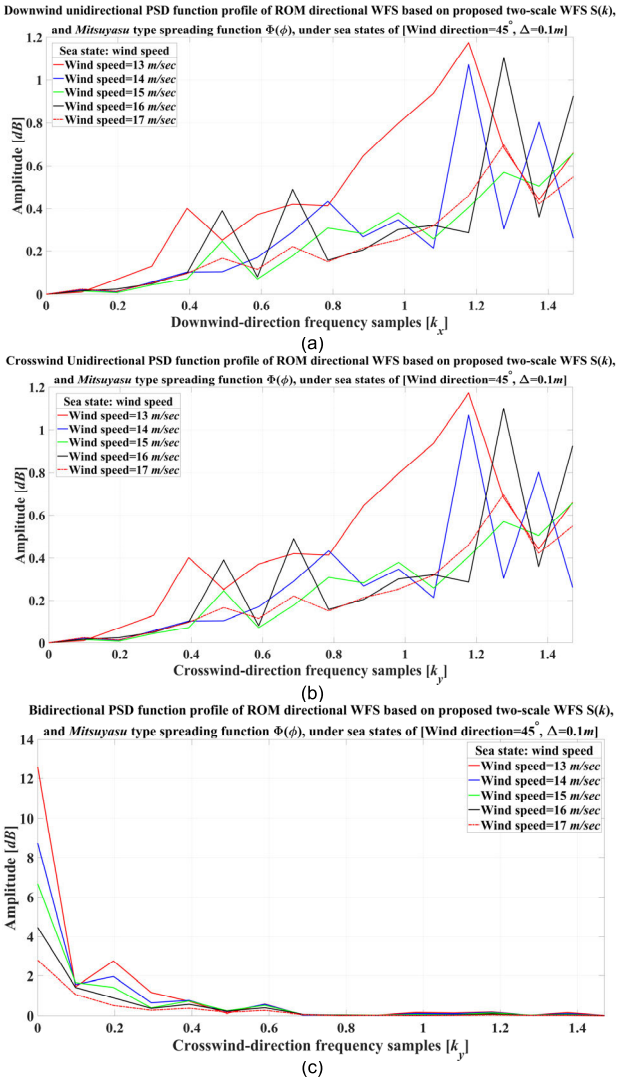

FIGURE 13. PSD function profile of ROM directional WFS based on fixed wind direction and variable wind speeds using Mitsuyasu spreading function type in the (a) Downwind-direction, (b) Crosswinddirection, (c) Bidirectional.

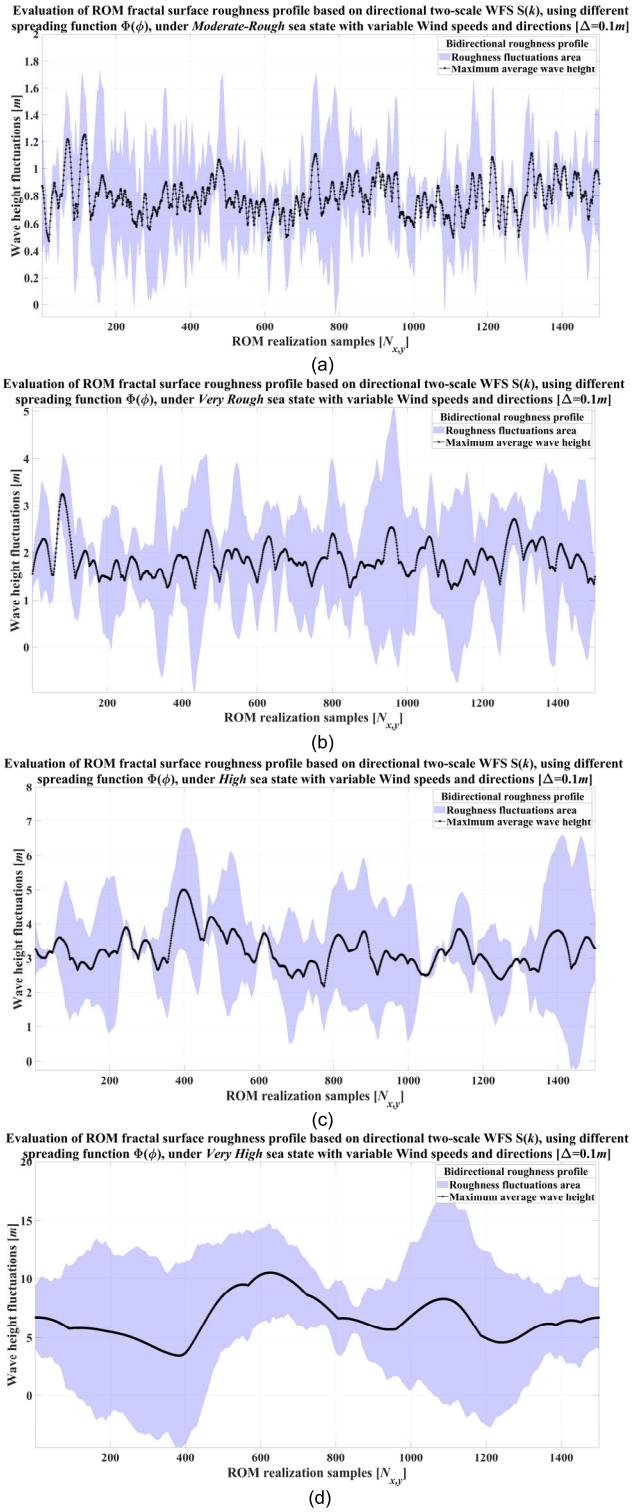

FIGURE 14. ROM surface roughness profiles based on different spreading functions under varying sea states including variable wind speeds and wind directions (a) moderate-rough, (b) very rough, (c) high, (d) very high sea states.

sea states but with different spreading functions undergo roughness enhancement via CNN. Subsequently, the LP decomposes the reconstructed roughness, and the LGE fusion strategy fuses the enhanced structural features. The fused roughness model is then output by the Laplacian inverse transform. This MTD fusion scheme can refine texture and preserve wave pattern, addressing challenges in multi-mode ROM fusion [150]. The upcoming section describes the proposed CNN roughness reconstruction [129], the LGE strategy [126], pyramidal fusion [127], and implementation scenario [150]. However, design details exceed the scope of this survey, and further instructions on architecture and training scenarios are available in [125] and [150].

1) CNN RECONSTRUCTION, LP FUSION, AND LGE STRATEGY

As per the proposed method depicted in Fig. 15, the CNN used in MTD fusion is designed to be a deep super resolution (DSR) network with 20 convolutional layers and 20 rectified linear unit (RLU) activation layers [129]. Each convolutional layer features a 3×3 kernel size, 1×1 the padding, and 1×1 stride, ensuring an output size identical to the

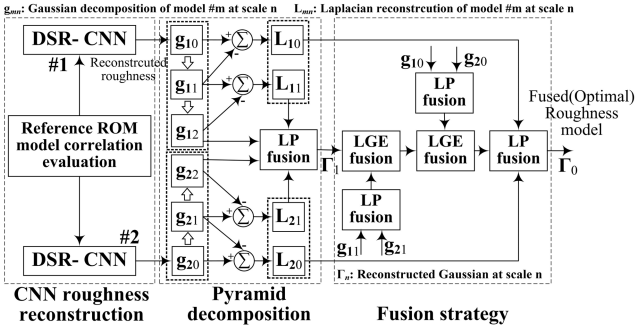

FIGURE 15. ROM optimal roughness model generation based on proposed MTD fusion scheme.

input. Furthermore, the constant gradient of the non-negative part in RLU prevents the vanishing gradient problem during training, thereby maintaining stable convergence rates, while the RLU itself significantly enhances training speed. The primary objective is to optimize the learning to predict an estimate of the input ROM, aiming to minimize the mean square errors (MSE) averaged over the training, serving as the loss function. The training consists 500 iterations, with a fixed learning rate of 0.0001, concluding upon the designated number of iterations. In essence, incorporating the DSR network into the solution enhances the reconstructed roughness by increasing residual information over the input ROM model, which is advantageous when dealing with a nondeterministic surface texture characterized by fractal roughness fluctuations. Following this, the proposed fusion scheme incorporates LP fusion, a pattern-sensitive approach that decomposes the reconstructed ROM models into various components using a set of transform functions and fuses them through a recursive algorithm, creating a multi-scale representation of ROM [124], [125], [127], [150]. The process begins with constructing a pyramid decomposition for each reconstructed roughness, followed by pyramidal fusion at each decomposition level based on the feature selection decision, which is designed to be an averaging mechanism. This mechanism reduces disparities and enhances data consistency, especially when reference ROM models share similar structural information, making it well-suited for wave pattern fusion, especially in textured area. The multi-scale pyramidal approach involves three major tasks, including LP decomposition, LP fusion, and LP reconstruction [150]. It's worth noting that the pyramidal approach in this research employs three layers of operation with g_{mn} representing Gaussian decomposition of input model m at scale n, L_{mn} for Laplacian reconstruction of input model m at scale n, and Γ_n for the reconstructed Gaussian model at scale n [125].

The fusion strategy is the final component of the proposed MTD fusion scheme. Given the inherent fractal properties of ROM roughness spread across the surface with varying fluctuation rates, the fusion rule must effectively capture the most relevant structural features of the ROM while minimizing disparities, resulting in the adoption of the LGE strategy. This strategy outperforms many other fusion rules for ROM

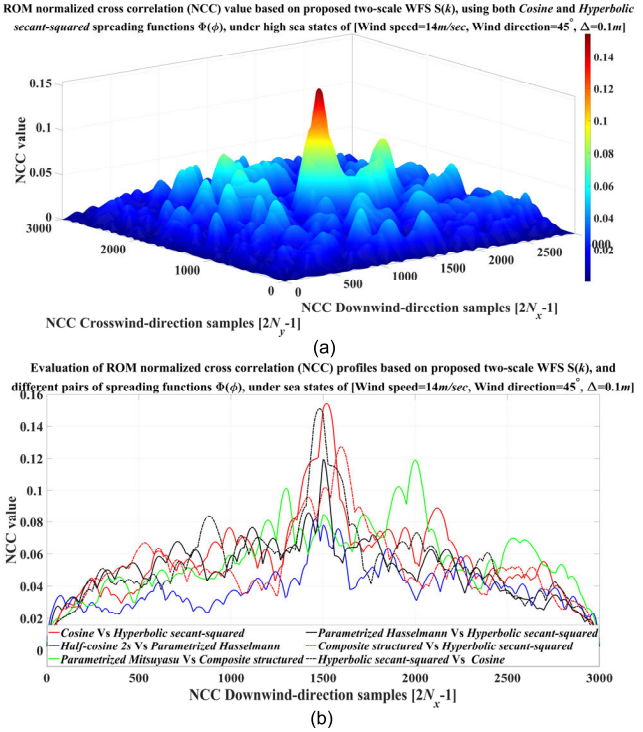

FIGURE 16. NCC profile evaluation under high sea state with wind speed 14 m/sec of and direction of 45 degrees (a) 3D view of NCC between cosine and hyperbolic secant-squared type applications, (b) 2D profile presentation of maximum NCC values using different pairs of spreading functions.

texture, thanks to its accurate detection of roughness fluctuations, effectively reduces disparities. When dealing with the decomposed models, a 3×3 window is defined around each coefficient value, and the local energy of the center coefficient is computed as the sum of squares of all coefficients within the window. By moving this window across the model, the local energy of all other coefficients in the decomposed model is determined [125]. If the local energy of the center coefficient is high, indicating roughness fluctuation referred to as wave height edge, it affects the center and its surrounding coefficients. Consequently, the local energy values of the reconstructed roughness and the decomposed model are compared, and coefficients with higher local energy values are selected using the LGE strategy [125]. This selection process ensures that the fused roughness model contains minimal errors compared to other single coefficient-based fusion rules. The entire MTD fusion scheme for optimal roughness model generation, including the DSR network, LP fusion, and LGE strategy, is depicted in Fig. 15, while specific implementation details can be found in [124], [125], [126], [127], and [150].

2) OPTIMAL ROUGHNESS MODEL FUSION SCHEME

To initiate the fusion scheme, the first step involves subjecting all input ROM models to cross-correlation assessment. A pair of highly correlated models is then selected to be fed into the DSR network. Notably, the reference ROM models must be derived under the same sea state conditions, ensuring

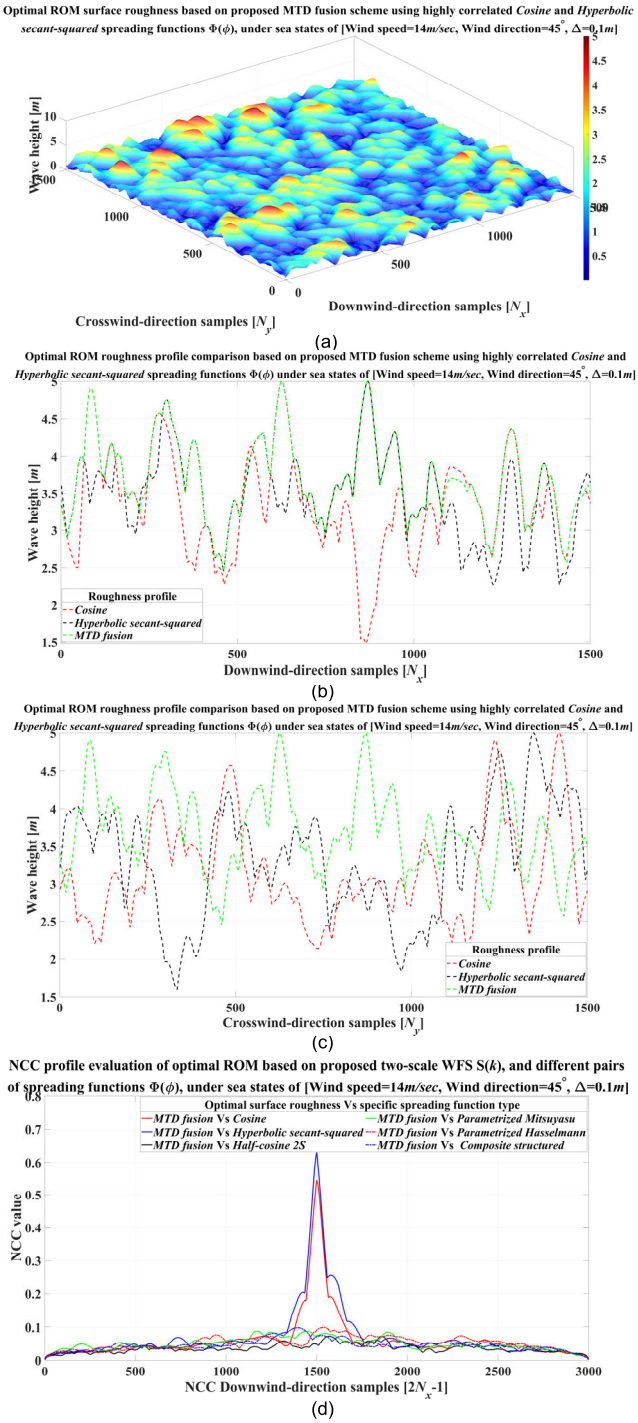

FIGURE 17. Evaluation of optimal ROM surface roughness model (a) 3D view of the reconstructed roughness map, (b) height profile comparison in downwind direction, (c) height profile comparison in crosswind direction, (d) NCC profile comparison of optimal ROM model with other models.

each sea state has its unique set of scattering distribution mode necessary for fusion. Based on the DSR network's learning rate, which is set to 0.0001, and a training iteration of 500 using the MSE convergence criteria, once the training process is completed, the residual information derived from each layer of the DSR network is integrated into the input ROM model [126]. As a result, the input ROM models are reconstructed, generating a refined output that captures the essential fractal characteristics under specified sea state conditions. Remarkably, the reconstructed ROM remains the same size as the input, and as the number of layers increases, the residual information becomes more distinct. After the CNN step, the MTD fusion scheme is applied using pyramidal decomposition illustrated in Figure 15 [125]. The fusion rule combines the LGE strategy and LP fusion to merge various coefficients of corresponding decomposition layers, resulting in an optimized roughness model through inverse Laplacian transform [127]. However, increasing decomposition layers heightens susceptibility to roughness fluctuations and computational costs. To strike an optimal balance, 3 decomposition layers are chosen, utilizing a Gaussian window of 3, similar to the LGE strategy, and a smoothing factor of 0.3 [126]. It is essential to note that during decomposition, down-sampling and up-sampling are carried out to maintain input ROM size throughout the fusion routine.

As per the proposed fusion scheme, two scenarios for generating optimal roughness model are introduced here. The first scenario reconstructs the optimal roughness model under an average sea state, specifically a high sea state with a wind speed of 14 *m*/*sec* and a wind direction of 45 degrees. In the second scenario, an extension of the results presented in Fig. 14, optimal fractal roughness profile are generated for moderate-rough, very-rough, high, and very-high sea states with varying wind speeds and directions. In the first scenario, the selected highly correlated ROM models, cosine and hyperbolic secant-squared spreading functions, exhibit a maximum normalized cross correlation (NCC) value of 0.15, as depicted in Fig. 16(a). Despite some minor peaks observed around the center due to the low NCC value, it remains the highest value among any other pair of spreading functions for this scenario, as shown in Fig. 16 (b). Notably, attaining a maximum NCC value of 1 for ROM surface roughness is an extreme case due to its time-varying characteristics caused by directional WFS formulations, resulting in fractal structural differences in both roughness and pattern. Following the selection of two highly-correlated ROM models, the MTD fusion depicted in Fig. 15 is executed, resulting in optimal ROM surface roughness displayed in Fig. 17(a).

The results in Figs. 17(a) to 17(c) further demonstrate the successful reconstruction of the optimal roughness model by the fusion scheme in both downwind and crosswind directions based on profile comparison. Both downwind and crosswind roughness profiles have been accurately restored, effectively capturing wave pattern characteristics from the input models with remarkable refinement. As observed in Figs. 17(b) and 17(c), the fusion scheme preserves the minimum and maximum ocean wave heights while refining the roughness fluctuations based on the input ROM models. This ensures that the reconstructed ROM model maintains consistency with the sea state classifications concerning the maximum wave height, resulting in the optimal ROM model. The simulation results in Fig. 17(d) further support this claim, revealing a significant increase in the NCC value of the

optimal roughness from 0.15 to approximately 0.7, indicative of the scheme's effectiveness in handling time-varying roughness patterns. It is important to note that although the proposed fusion scheme may yield high NCC values when applied to other input pairs of spreading functions, the resulting NCC value may not be as high as demonstrated in Fig. 17(d), as those models are not highly correlated. Thus, the maximum achievable NCC of the proposed MTD fusion scheme heavily relies on using highly correlated ROM models as input. However, uncertainties remain regarding whether the MTD fusion retains the scattering pattern and orientation as defined by the spectral distribution mode under sea state conditions.

To investigate directionality effects, employing a tensor field descriptor (TFD) map for structural surface tension synthesis would be valuable in assessing roughness pattern and wave height orientation within the reconstructed optimal ROM model, compared to its reference input models [151]. The TFD map serves as an effective tool to summarize prevalent geometrical directions of surface roughness gradient in a given vicinity of samples, along with coherence degree in those directions [152]. Essentially, the TFD map represents a normalized surface tension matrix visualizing partial derivatives of roughness geometrical information and their scattering distribution mode, providing valuable insight into roughness pattern orientation. TFD maps are generated for both the reference input ROM model with a cosine type spreading function and the reconstructed optimal ROM model, depicted in Fig. 18. The blue vector indicates areas with low texture coherency or surfaces with normal tension within the ROM model, while red vectors represent surface wave height fluctuations with higher entropy, commonly known as highly-textured areas. As can be seen, the vectorial axes are oriented in specific direction, indicating coherency with neighboring samples and collectively revealing the dominant scattering pattern orientation.

Upon analyzing Figs. 17 and 18, along with fractal roughness fluctuations manifesting as ocean wave height alterations, some partial differences are observed between the input models and the optimal ROM model after fusion. However, It is noteworthy that the main textural pattern orientation aligns in the same direction for both the optimal ROM model and the input reference ROM models, initially set at 45 degrees. This indicates that the proposed MTD fusion effectively preserves the wave pattern orientation, specifically the scattering orientation, while refining the roughness information. It is crucial to emphasize that while the proposed MTD fusion is not the exclusive technique for generating an optimal ROM roughness profile, any fusion scheme used must satisfy two vital criteria, including fine pattern refinement and preservation of scattering distribution mode, particularly scattering orientation, which are characteristics typically found in pattern-sensitive fusion techniques. In the second scenario, the same fusion scheme used in the previous results is applied, investigating the results of Fig. 14 representing four major sea states with varying wind

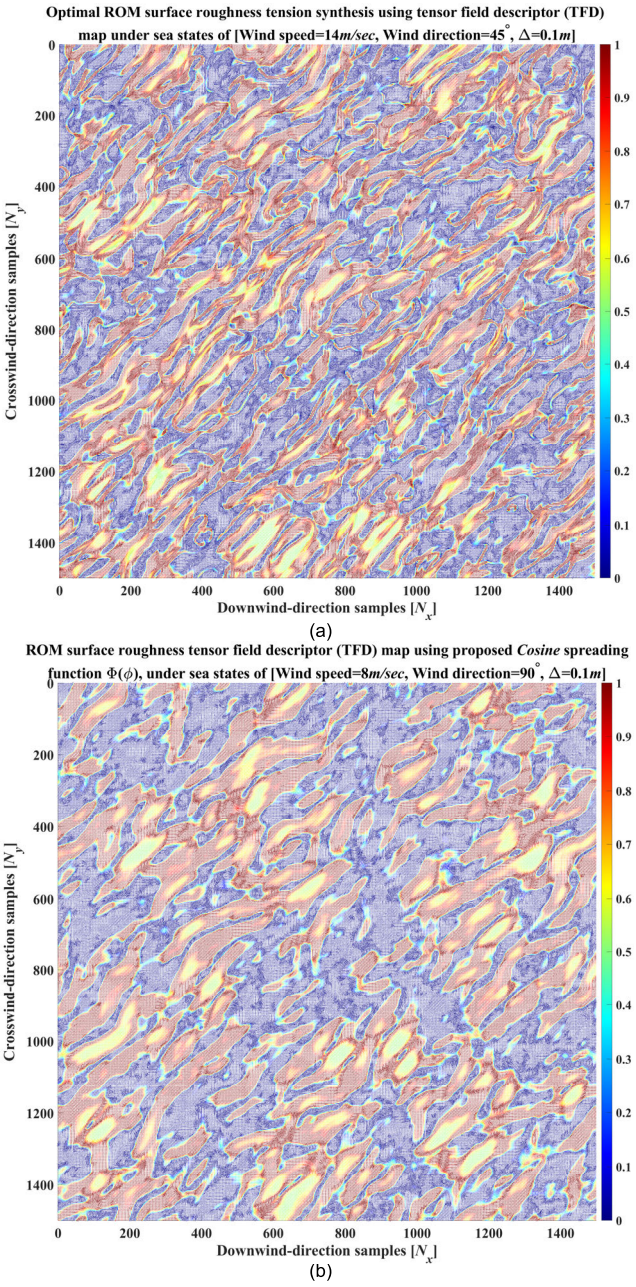

FIGURE 18. Evaluation of ROM surface roughness tension synthesis based on TFD map investigation under high sea state condition with wind speed 14 m/sec of and direction of 45 degrees (a) Optimal ROM (b) Reference input ROM based on cosine type spreading function.

speeds and directions. The objective of this optimal roughness profile evaluation is twofold. Firstly, to provide optimal roughness profile for estimating the wave height profile without considering spreading functions in the fusion process. Secondly, to utilize the optimal profile for electromagnetic interaction investigations, focusing on the surface roughness profile rather than solely on spectral functions. To achieve this, the output ROM models from Fig. 14 serve as input for the proposed fusion scheme. Due to the high correlation criteria, the number of output models is reduced to one-sixth. However, this reduction does not hinder optimal roughness

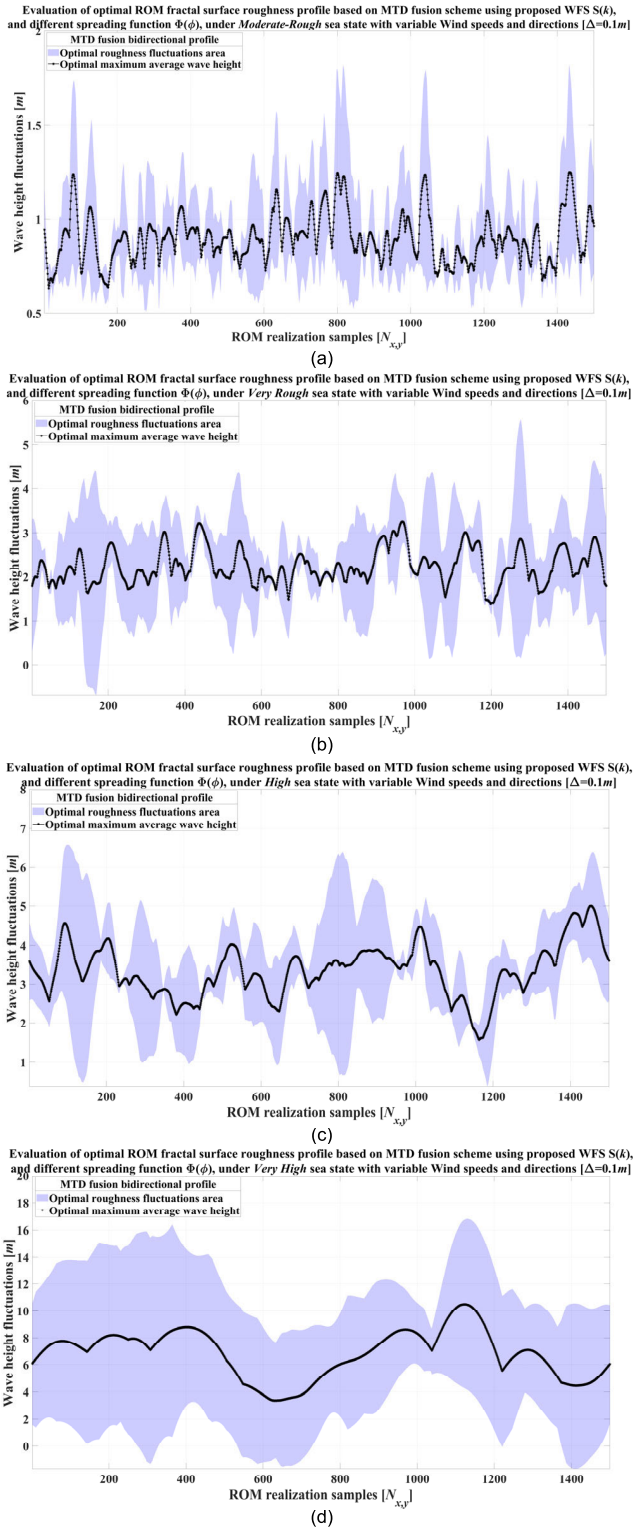

FIGURE 19. Optimal ROM roughness profiles based on MTD fusion using different spreading functions under varying sea states with variable wind speeds and directions (a) moderate-rough, (b) very rough, (c) high, (d) very high sea states.

profile generation, as the primary goal is to find an optimal pattern matching sea state rather than specific spreading functions. The resulting optimal roughness profiles for different sea states are presented in Fig. 19. Comparing these results to Fig. 14, the optimal counterparts exhibit fewer rapid wave height alterations and narrower fluctuation areas due to the fusion scheme, resulting in a more consistent model.

Importantly, both scenarios exhibit the same maximum ocean wave heights, aligning perfectly with the directional WFS formulations and sea state classifications. This demonstrates the successful preservation of critical characteristics by the fusion scheme while improving fine roughness details to match optimal patterns for various sea state conditions. The comparison between the results in Figs. 14 and 19 further highlights that MTD fusion not only refines roughness information but also preserves its scattering distribution mode, valuable for investigating backscattering properties. Thus, the following section will explore ROM texture roughness and its electromagnetic interactions from the SAR perspective, specifically comparing the backscattering profiles of the reference ROM model and the optimal profile derived through the fusion scheme.

B. ROM OPTIMAL SAR RAW DATA GENERATION BASED ON HYBRID-DOMAIN INVERSE PROBLEM SOLUTION

The backscattering properties of the ocean surface are valuable for radiometric calibrations, particularly in SAR image reconstruction. However, due its time-varying characteristics, dynamic structure, and composite spectral distribution influenced by sea states, the precise contribution of ROM surface to electromagnetic interactions remains largely unestablished. This is mainly due to the lack of a comprehensive reference dataset, necessitating extensive field surveys and detailed experimental measurements, tasks often impractical in real-world settings. In contrast, the proposed ROM models and fused optimal model offer an alternative approach to studying ocean electromagnetic interactions without relying on field experiments. However, to conduct such backscattering analysis, it is essential to generate a dataset that aligns with both SAR observation geometry and IFA. In this process, the ROM surface is regarded as the terrain to be imaged, with its roughness values being mapped to complex image samples under SAR observation geometry while maintaining the original aspect ratio. Each sample is then interpreted as the SAR pixel intensity based on its grayscale range. Terrain adaptation plays a crucial role in this transformation, ensuring that ROM backscattering entities remain unchanged while adjusting intensities and attributes affected by system parameters and observation geometry through zero padding and surface reflectivity stretching. Moreover, normalization is employed to ascertain the lower and upper bounds of the array, thereby yielding a complex homogeneous ROM terrain. Subsequently, following the model transformation and texture adaptation, the incoherent information from the reference transformed grayscale image of ROM is imported into the RDG step, as depicted in Fig. 20.

The RDG in this study employs an inversed equalized hybrid-domain algorithm based on the SAR system parameters listed in Table 2, with some directly and indirectly

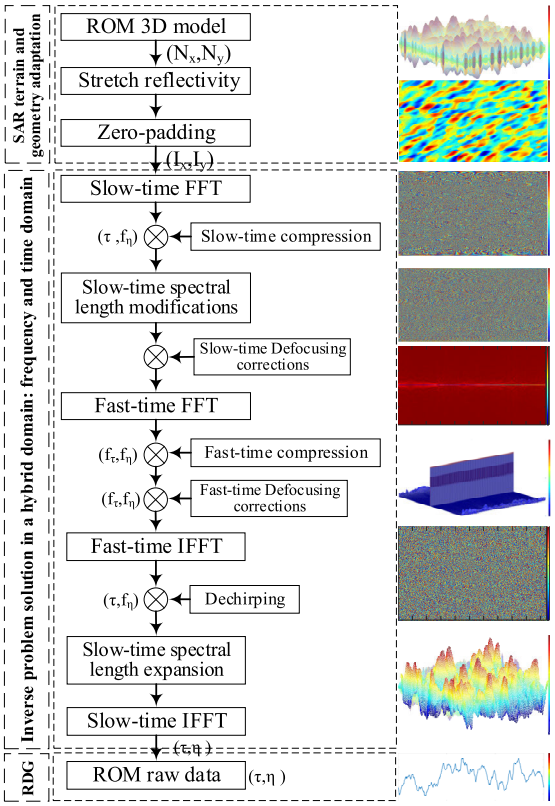

FIGURE 20. Optimal ROM raw data generation routine based on inverse pr oblem solution using a hybrid-domain algorithm.

TABLE 2. SAR system parameters for RDG extraction.

Parameter	Value
Carrier frequency	9.2 GHz
3dB Bandwidth	60 MHz
Pulse width	0.4 μsec
Duty cycle	0.2
Scaling factor	1
Repetition frequency	4 KHz

TABLE 3. ROM texture SAR image evaluations under high sea state of 14 *m/sec* and 45 degrees.

ROM model	PSLR [dB]	ISLR [dB]	SNR [dB]
Cosine type	-13.35	-13.13	17.61
Hyperbolic secant	-13.57	-14.47	17.07
Optimal ROM	-13.54	-15.13	15.38

determined by the ROM size [122]. The normalized SAR received backscattered data is derived using the procedure in Fig. 20 and the two optimal roughness generation scenarios in Section VI. A. 2, used for MTD fusion, to verify the results and generate their optimum backscattered profile. Table 3 presents SAR texture objective metrics based on peak side-lobe ratio (PSLR) and integrated side-lobe ratio (ISLR) estimation, showing that the provided texture adaptation in the proposed inverse problem solution meets the RDG requirements, with no specific spreading function consistently outperforming the other. Both the cosine and

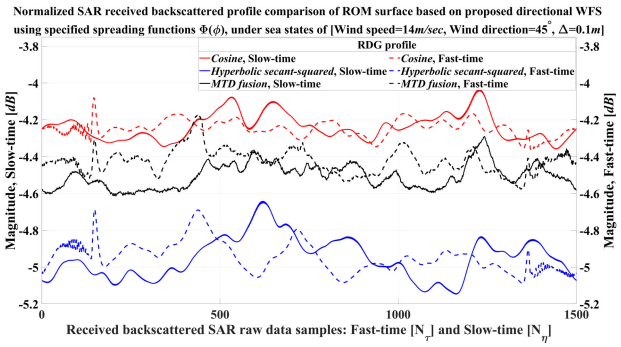

FIGURE 21. Comparison of the received backscattered profile of the optimal ROM surface roughness in fast-time and slow-time with its reference models based on cosine and hyperbolic secant-squared spreading functions.

hyperbolic secant-squared types exhibit MSE of 0.02 and peak signal-to-noise ratio (SNR) of 16.63 *dB* when compared to the optimal texture, despite slightly different SNR values. The SAR terrain adaptation is followed by the extraction of the spatial resolution profile, involving an active evaluation of sensor-terrain interactions in the form of phase history using the remaining steps of Fig. 20. The RDG results in Fig. 2 show a maximum backscattered magnitude of the terrain reflectivity in the fast-time direction of -4.03 *dB* for the cosine type spreading function, -4.64 *dB* for the hyperbolic secant-squared type, and -4.29 *dB* for the optimal roughness model. Similarly, in the slow-time direction, they are -4.03 *dB*, -4.59 *dB*, and -4.17 *dB*, respectively. The optimal ROM roughness exhibits a received signal strength enhancement of approximately 0.5 *dB*, as shown in Fig. 21. It is noteworthy that the attenuation in the received signal strength of the reference ROM models stems from the undulating ocean terrain, resulting in spectral interactions that may cause information loss in the dataset.

However, MTD fusion not only mitigates these attenuations by up to 0.5 *dB* but also provides an alternative optimal roughness, which is particularly valuable. Despite the advantages of an optimal model retaining scattering information, obtaining a comprehensive spatial resolution profile of the ROM concerning sea state is challenging due to the limited information capacity per resolution cell and the time-varying nature of the surface, leading to discrete signal returns and potential data loss. Therefore, acquiring a thorough spatial resolution profile of ROM, covering all potential roughness fluctuations, is essential for understanding electromagnetic interactions on the ocean surface and the associated information loss. To address this challenge, the second RDG evaluation scenario utilizes optimal ROM roughness profiles from Fig. 19, extracting normalized SAR received backscattered profiles under varying sea state conditions, including moderate-rough, very-rough, high, and very-high sea state conditions, with considerations for wind speeds and directions. This profile extraction serves two main purposes. Firstly, it provides an approximate profile of ROM backscattering under different sea states independent of

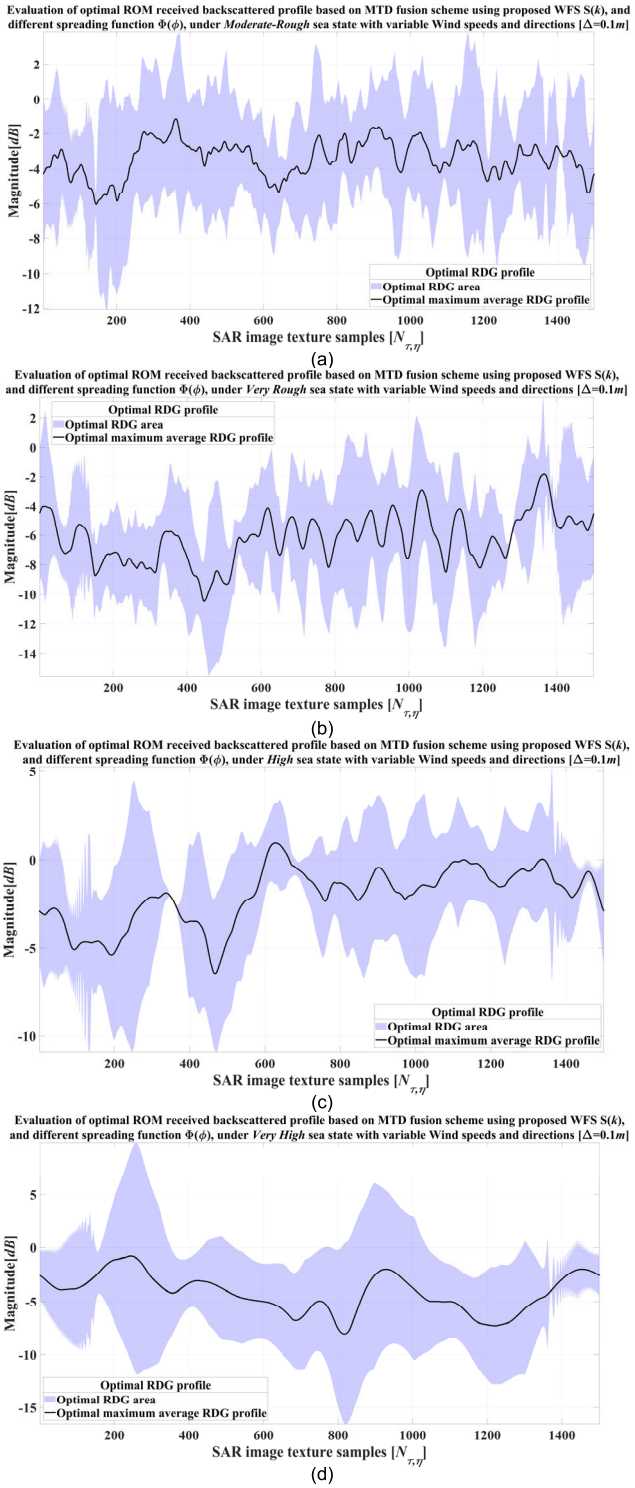

FIGURE 22. Evaluation of optimal ROM surface roughness received backscattered profiles based on MTD fusion under varying sea states with variable wind speeds and directions (a) moderate-rough, (b) veryrough, (c) high, (d) very-high sea states.

directional WFS formulations. Secondly, it aids in SAR link budget calculation, ensuring compliance with ROM roughness behaviors across varied sea states, crucial for accurate ocean texture interpretations. As a result, utilizing the optimal ROM models from Fig. 19 as input for the RDG scenario,

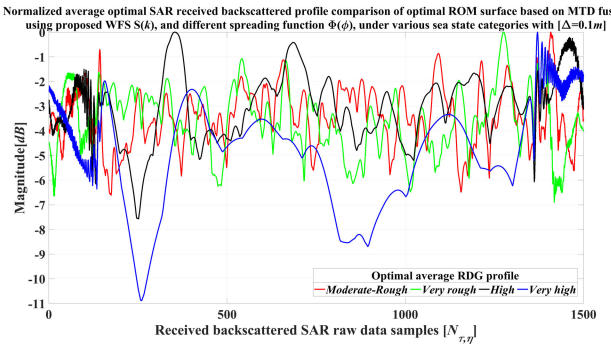

FIGURE 23. Comparison of optimal ROM received backscattered profile under varying sea states with variable wind speeds and directions.

TABLE 4. Optimal ROM models RDG profile evaluation based on intra sea state conditions.

Profile intensity	Physical sea state conditions			
	Moderate-rough	Very-rough	High	Very-high
Intra-attenuation [dB]	4.91	7.48	7.73	7.88
Max. Ampl. Diff. [dB]	6.61	6.89	7.46	10.88

Fig. 22 showcases the relevant optimal RDG profiles of ROM under various sea states with varying wind speeds and directions, independent of spreading functions. Observing Fig. 22(a) to 22(d), as sea state conditions progress from moderate-rough to very-high, accompanied by increasing wind speed and direction changes, the optimal RDG area widens and strengthens, while its change rate slows and takes a smoother trend. This backscattering behavior highlights the spectral interactions between directional WFS components, encompassing both long and short waves, affecting electromagnetic interactions across varying sea states. It suggests that asymmetrical roughness fluctuations, influenced by spectral properties, coupled with centrosymmetric angular spreading of waves, pose challenges in establishing a deterministic backscattering profile solely based on sea states. The results in Fig. 22 reaffirm that high sea states with strong wind speeds predominantly exhibit a dominant texture characterized by long waves, which smooth out small roughness variations and diminish rapid intensity alterations in the RDG profile.

Conversely, lower sea states with lower wind speeds are affected by short-wave structures, leading to frequent roughness alterations and rapid signal intensity variations. Consequently, lower sea states are more susceptible to signal intensity attenuations resembling random noise, increasing likelihood of SNR degradation and SAR image anomalies. Higher sea states, on the other hand, with smoother but stronger profiles risk a drop in received signal level, impairing signal integrity, causing information loss, and degrading image resolution [147]. It is important to note that the SAR sensor observes ROM texture reflectivity directly, manifesting as spatially varying quantities, potentially resulting in abnormal intensity variations in the spatial resolution profile and texture inconsistencies, particularly at higher resolutions. Figure. 23 compares the average

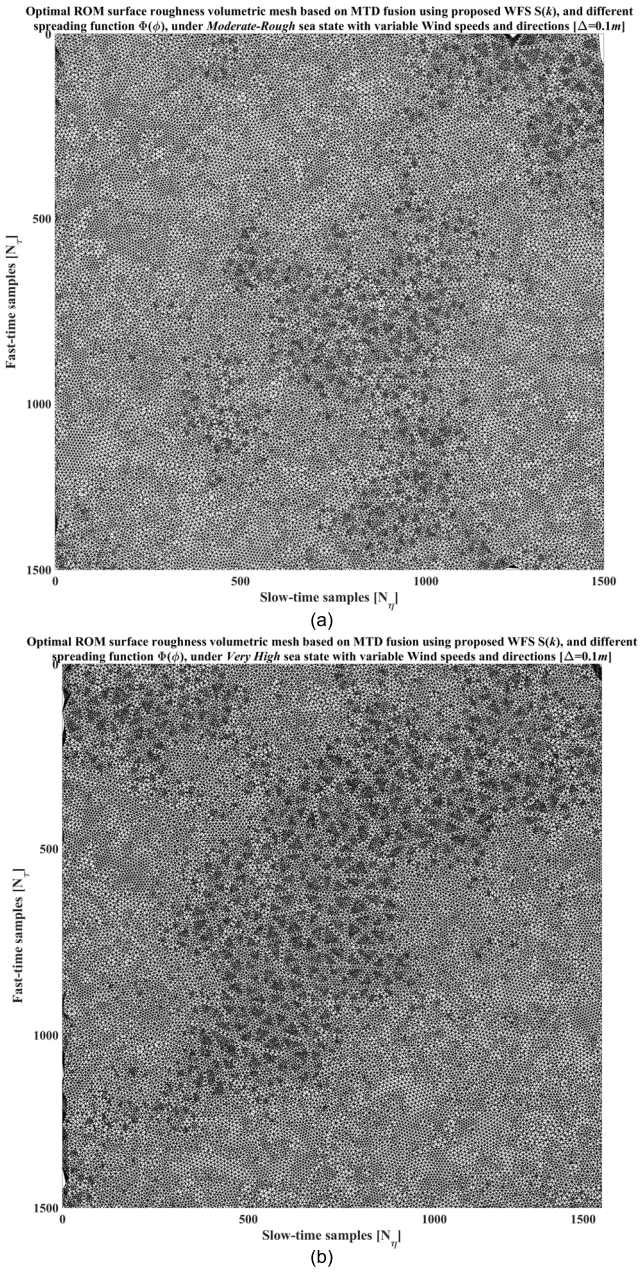

FIGURE 24. Volumetric mesh evaluation of optimal average ROM surface roughness based on MTD fusion (a) moderate-rough, (b) veryhigh.

normalized received backscattered profile of the four categorized sea states depicted from Fig. 22, indicating an increase in maximum magnitude difference as sea states progress from moderate-rough to very-high, driven by the dominant effects of long waves. Moderate and very-rough sea states mostly suffer from rapid signal intensity variations caused by small-wave modulations, resulting in different amplitude profiles. To provide a detailed demonstration, Table 4 provides an intra-sea state condition evaluation, detailing maximum amplitude difference and attenuation within each categorized sea states using the profiles from Fig. 22. The results reveal significant variations in signal reflectivity and attenuation among different sea states. Very-high sea states exhibit the highest reflectivity difference of 11 *dB*, primarily due to the dominance of long waves, along with the greatest attenuation of nearly 8 *dB* in response to wave height changes, resulting in broader RDG areas and increased SNR degradation. Very-rough and high sea states display similar intra-state properties, with average attenuations and maximum amplitude differences around 7.5 *dB* and 7.2 *dB*, respectively. In contrast, the moderate-rough sea state shows less attenuation and a smaller maximum amplitude difference, approximately 5 *dB* and 6.5 *dB*, respectively. The same evaluation is conducted for inter-state properties, showing that the difference in average attenuation between the moderate-rough and very-high sea states is approximately 9.73 *dB*, with the maximum difference in average amplitude being 4.9 *dB*, indicating that higher sea states have stronger reflectivity while also suffering from higher attenuation than the lower sea states. The amplitude difference between very-high and very-rough sea states is 4.1 *dB* with a 9.2 *dB* attenuation, whereas it is about 3.3 *dB* with an 8.7 *dB* attenuation for very-high and high sea states.

The observable features of the ROM texture that best explain the origin of inter and intra-backscattering properties are roughness fluctuations, including large-scale and small-scale wave breakings or microbreakers, induced by both waves and non-linear interactions among them. Remarkably, all optimal ROM models experience roughness fluctuations due to the random entity of WFS components in response to sea states, and no sea state follows a specific trend in the resolution profile. In other words, the changes in both inter and intra-sea states is relative; however, the likelihood of observing similar spectral behavior and roughness fluctuations under the same category of sea state is higher compared to different categories. To further support this claim, Fig. 24 presents volumetric mesh representation of surface roughness for both the optimal average moderate-rough and very-high sea states, as displayed in Figs. 19(a) and 19(d). In this visualization, roughness samples are converted into a triangular network based on triangulation structure, consisting of vectors defining roughness vertices, and a continuous tetrahedral mesh connecting them based on ocean wave height values. Smaller triangle concentrations indicate rapid changes in ROM roughness or intense fluctuations in wave heights within the specified cell size, while larger triangles signify more homogeneous texture behavior with slower changes. More specifically, dense clusters of small triangles represent high entropy regions within the texture, known as ROM highly textured areas, which undergo rapid ocean wave breakings and signal intensity variations. These highly-textured regions are the source of pixel anomalies and are susceptible to alteration over time, demonstrating the stochastic features of ocean wave spectra. Therefore, in fully developed ROM conditions, longer waves tend to propagate in the direction of the wind, while smaller waves exhibit more isotropic behavior. To summarize, each sea state condition redistributes energy through physical ocean wave scatterings, resulting in stochastic directional coupling effects that not only generate

a distinct pattern of fractal roughness but also lead to specific variability in the surface wave pattern.

On the other hand, the identification of such variations in scattering patterns, including fractal roughness, embedded fluctuations, spectral distribution mode, and pattern orientation, has become crucial in understanding pattern realization and quantitatively predicting ROM roughness and its backscattering properties. The results further demonstrated that the proposed pattern-sensitive fusion approach effectively reconstruct optimal models and facilitates investigation into ROM electromagnetic interactions.

VII. CONCLUSION

Given the significant ramifications of climate change on ocean sustainability, accurate observation of ocean environments and provision of precise, reliable, and up-to-date data for global studies are imperative. Advancements in remote sensing enable observation of Earth's surface and oceans across diverse spatio-temporal scales and imaging resolutions, facilitating extensive remote sensing of oceans and detailed insights into associated processes. The ocean WFS formulation serves as the fundamental portrayal of ocean surface structure, providing valuable information about wind-generated wave statistical distribution and significantly contributing to ocean predictions and surface roughness interpretations. However, significant insight remain unexplored in oceanic hydrodynamics and structural properties, particularly from the SAR perspective, due to the time-varying surface characteristics resulting in data disparities between sensor designers and oceanographers regarding wave height measurements. Accurate modeling of ROM roughness is crucial for understanding surface structural characteristics and complex interactions within sea state context, including factors like wind speed and direction. Despite efforts, many ROM models overlook the directional spreading's influence on wave height distributions, necessitating a comprehensive portrayal beyond relying solely on wind speed-based wavefield scattering. Additionally, existing models often underutilize spectral interactions and wave pattern characteristics, focusing primarily on one-dimensional directional WFS. In essence, understanding prevailing sea state conditions, including both wind speed and direction, is essential for robust ROM surface roughness modeling and SAR interpretation, as they significantly influence spectral scattering distribution and wave patterns.

The present research investigates the angular distribution of energy scattering in ROM, focusing on the impact of sea states on directional WFS and its role in surface roughness modeling. By formulating ROM spectral component distributions using established spreading functions, the study analyze evolving surface interactions, revealing a balance between directional distributions and spectral scatterings. This equilibrium yields a comprehensive composite ROM surface, providing insights into wave pattern fractal properties. Wind-generated waves, influenced by sea states, undergo energy variations, prompting the synthesis of spreading functions based on distinct scattering distribution modes in composite ROM models. Wind direction, in conjunction with spreading functions, emerges as a more indicative factor of distribution modes compared to surface elevation, while wind speed predominantly governs wave heights. The interplay between directional WFS and sea states significantly influences the manifestation of intricate fractal roughness fluctuations inherent to ROM surfaces. To explore this, ROM models were investigated using a three-fold approach. Firstly, comparing ROM modeling via directional WFS formulations with different spreading functions under varied sea state conditions. These conditions were categorized into five distinct groups, each defined by specific wind speed ranges from $7m/s$ to 24 m/s and directions spanning 90 degrees from downwind to upwind. The resulting profiles of maximum, minimum, and average ocean wave heights corresponding to these designated sea states were precisely simulated, and subjected to in-depth analysis. Subsequently, the MTD fusion algorithm, a pattern-sensitive fusion technique, was developed to deduce and explore optimal roughness profiles for each sea state. This fusion method ensures optimal profile estimations and roughness predictions while preserving texture pattern orientations, crucial for investigations. Notably, it extends seamlessly to other ROM models with diverse spreading functions under varying sea states, producing an optimal roughness profile aligned with the research scope. Finally, a comparative assessment was undertaken between the electromagnetic interaction profiles of the two roughness profiles, including the realized ROM model and its correspondent optimal fused one, using an inverse problem solution. The provided RDG profile highlights that fractal roughness fluctuations, whether within the ROM model or its optimal counterpart, involve phenomena such as large-scale wave breaking and small-scale microbreakers, contributing to both inter- and intra-backscattering properties. This implies that the optimal fused roughness reduces the need for extensive simulation, offering a similar optimal response to distinct roughness properties demonstrated by applying different spreading functions under varying sea states.

In conclusion, diverse sea states coordinates the redistribution of ocean wave energy through spectral scatterings, resulting in distinctive directional WFS properties that manifest discernible wave patterns in the ROM characterized by significant wave height fluctuations and directions. Precise characterization of these complex fractal properties is essential for successful ROM modeling and comprehensive understanding of their intricate backscattering attributes. This literature survey, in its succinct form, offers an objective assessment through modeling, synthesis, and analysis stages. Complemented by an extensive array of references, it aims to provide readers with an in-depth grasp of the intricate nuances underpinning ocean spectral scatterings, directional influences, and their consequential electromagnetic interaction properties.

Looking forward, several avenues for enhancement present themselves, including (a) the integration of ships into the

ROM modeling and the consideration of target detection within SAR images, (b) assessing the motions of both target and platform to facilitate spatiotemporal image reconstruction of ROM, (c) the systematic assessment of the SAR radio link budget analysis to refine ROM observation and IFA, (d) the exploration of methodologies for clutter analysis and its suppression, the optimization of the modeling routine, and (f) the exploration of alternative spreading functions and fusion techniques to further enrich the evaluation process. Consequently, the continuation of this survey endeavors to unravel deeper insights into sea states and composite ROM roughness models, thereby bestowing valuable contributions to the realm of ocean remote sensing and radar probing.

ACKNOWLEDGMENT

The authors would like to thank Korea Polar Research Institute (KOPRI) for providing all facilities for this research.

REFERENCES

[1] T. T. Janssen and T. H. C. Herbers, "Nonlinear wave statistics in a focal zone," *J. Phys. Oceanogr.*, vol. 39, no. 8, pp. 1948–1964, Aug. 2009.

[2] S. Elgar, "Waves in oceanic and coastal waters," *Oceanography*, vol. 20, no. 3, pp. 133–135, Sep. 2007.

[3] A. Constantin, "Nonlinear water waves: Introduction and overview," *Phil. Trans. Roy. Soc. A, Math., Phys. Eng. Sci.*, vol. 376, no. 2111, Dec. 2111, Art. no. 20170310.

[4] A. Pecher and J. P. Kofoed, *Handbook Ocean Wave Energy*. Cham, Switzerland: Springer, 2017.

[5] P. A. Hwang, "A note on the ocean surface roughness spectrum," *J. Atmos. Ocean. Technol.*, vol. 28, no. 3, pp. 436–443, Mar. 2011.

[6] D. V. Chalikov, "Linear and nonlinear statistics of extreme waves," *Russian J. Numer. Anal. Math. Model.*, vol. 32, no. 2, pp. 91–98, Apr. 2017.

[7] S. M. Henderson and A. J. Bowen, "Observations of surf beat forcing and dissipation," *J. Geophys. Res., Oceans*, vol. 107, no. C11, p. 14, Nov. 2002.

[8] A. Hunt-Raby, I. K. Othman, R. Jayaratne, G. Bullock, and H. Bredmose, "Effect of protruding roughness elements on wave overtopping," in *Coasts, Marine Structures and Breakwaters: Adapting to Change*. London, U.K.: Thomas Telford Ltd, Jan. 2010, pp. 574–586.

[9] S. Li, Z. Zou, D. Zhao, and Y. Hou, "On the wave state dependence of the sea surface roughness at moderate wind speeds under mixed wave conditions," *J. Phys. Oceanogr.*, vol. 50, no. 11, pp. 3295–3307, Nov. 2020.

[10] D. T. Resio, C. E. Long, and C. L. Vincent, "Equilibrium-range constant in wind-generated wave spectra," *J. Geophys. Res., Oceans*, vol. 109, no. C1, Jan. 2004, Art. no. C01018.

[11] J. Thomson, E. A. D'Asaro, M. F. Cronin, W. E. Rogers, R. R. Harcourt, and A. Shcherbina, "Waves and the equilibrium range at ocean weather station p," *J. Geophys. Res., Oceans*, vol. 118, no. 11, pp. 5951–5962, Nov. 2013.

[12] R. S. Gibson and C. Swan, "The evolution of large ocean waves: The role of local and rapid spectral changes," *Proc. Roy. Soc. A, Math., Phys. Eng. Sci.*, vol. 463, no. 2077, pp. 21–48, Jul. 2077.

[13] T. Aderinto and H. Li, "Ocean wave energy converters: Status and challenges," *Energies*, vol. 11, no. 5, p. 1250, May 2018.

[14] J. Zhang and M. Benoit, "Wave–bottom interaction and extreme wave statistics due to shoaling and de-shoaling of irregular long-crested wave trains over steep seabed changes," *J. Fluid Mech.*, vol. 912, p. A28, Feb. 2021.

[15] Y. Fan, S.-J. Lin, I. M. Held, Z. Yu, and H. L. Tolman, "Global ocean surface wave simulation using a coupled atmosphere–wave model," *J. Climate*, vol. 25, no. 18, pp. 6233–6252, Apr. 2012.

[16] U. Högström, E. Sahlée, A.-S. Smedman, A. Rutgersson, E. Nilsson, K. K. Kahma, and W. M. Drennan, "Surface stress over the ocean in swell-dominated conditions during moderate winds," *J. Atmos. Sci.*, vol. 72, no. 12, pp. 4777–4795, Nov. 2015.

[17] P. A. Hwang, "Estimating the effective energy transfer velocity at air-sea interface," *J. Geophys. Res., Oceans*, vol. 114, no. C11, Nov. 2009, Art. no. C11011.

[18] A. Iafrati, "Energy dissipation mechanisms in wave breaking processes: Spilling and highly aerated plunging breaking events," *J. Geophys. Res., Oceans*, vol. 116, no. C7, pp. 1–22, Jul. 2011.

[19] I. R. Young and A. V. Babanin, "Spectral distribution of energy dissipation of wind-generated waves due to dominant wave breaking," *J. Phys. Oceanogr.*, vol. 36, no. 3, pp. 376–394, Mar. 2006.

[20] A. Herman, "Spectral wave energy dissipation due to under-ice turbulence," *J. Phys. Oceanogr.*, vol. 51, no. 4, pp. 1177–1186, Apr. 2021.

[21] A. Zavadsky, D. Liberzon, and L. Shemer, "Statistical analysis of the spatial evolution of the stationary wind wave field," *J. Phys. Oceanogr.*, vol. 43, no. 1, pp. 65–79, Jan. 2013.

[22] V. G. Polnikov and F. A. Pogarskiy, "Spectra of long-term series for wind speed and wave height in the Indian ocean area," *J. Geophys. Res., Atmos.*, vol. 122, no. 1, pp. 104–120, Jan. 2017.

[23] V. G. Polnikov, "Spectral description of the dissipation mechanism for wind Waves. Eddy viscosity model," *Mar. Sci.*, vol. 2, no. 3, pp. 13–26, May 2012.

[24] J. E. Stopa, F. Ardhuin, A. Babanin, and S. Zieger, "Comparison and validation of physical wave parameterizations in spectral wave models," *Ocean Model.*, vol. 103, pp. 2–17, Jul. 2016.

[25] T. S. Hristov, K. D. Anderson, and C. A. Friehe, "Scattering properties of the ocean surface: The Miller–Brown–Vegh model revisited," *IEEE Trans. Antennas Propag.*, vol. 56, no. 4, pp. 1103–1109, Apr. 2008.

[26] F. Nouguier, C.-A. Guérin, and B. Chapron, "Scattering from nonlinear gravity waves: The 'choppy wave' model," *IEEE Trans. Geosci. Remote Sens.*, vol. 48, no. 12, pp. 4184–4192, Dec. 2010.

[27] P. Janssen, *The Interaction of Ocean Waves and Wind*. Cambridge, U.K.: Cambridge Univ. Press, Oct. 2004.

[28] P. P. Sullivan and J. C. McWilliams, "Dynamics of winds and currents coupled to surface waves," *Annu. Rev. Fluid Mech.*, vol. 42, no. 1, pp. 19–42, Jan. 2010.

[29] G. Wu, C. Liu, and Y. Liang, "Comparative study on numerical calculation of 2-D random sea surface based on fractal method and Monte Carlo method," *Water*, vol. 12, no. 7, p. 1871, Jun. 2020.

[30] G. Wu, Y. Liang, and S. Xu, "Numerical computational modeling of random rough sea surface based on JONSWAP spectrum and donelan directional function," *Concurrency Comput., Pract. Exper.*, vol. 33, no. 15, Sep. 2019, Art. no. e5514.

[31] A. W. Fisher, L. P. Sanford, M. E. Scully, and S. E. Suttles, "Surface wave effects on the translation of wind stress across the air–sea interface in a fetch-limited, coastal embayment," *J. Phys. Oceanogr.*, vol. 47, no. 8, pp. 1921–1939, Aug. 2017.

[32] J. P. Grainger, A. M. Sykulski, P. Jonathan, and K. Ewans, "Estimating the parameters of ocean wave spectra," *Ocean Eng.*, vol. 229, Jun. 2021, Art. no. 108934.

[33] H. Mitsuyasu, "Reminiscences on the study of wind waves," *Proc. Jpn. Acad., Ser. B*, vol. 91, no. 4, pp. 109–130, 2015.

[34] A. Bringer, B. Chapron, A. Mouche, and C.-A. Guérin, "Revisiting the short-wave spectrum of the sea surface in the light of the weighted curvature approximation," *IEEE Trans. Geosci. Remote Sens.*, vol. 52, no. 1, pp. 679–689, Jan. 2014.

[35] Z. Huang, "An experimental study of wave scattering by a vertical slotted barrier in the presence of a current," *Ocean Eng.*, vol. 34, nos. 5–6, pp. 717–723, Apr. 2007.

[36] G. Dolcetti, K. V. Horoshenkov, A. Krynkin, and S. J. Tait, "Frequency-wavenumber spectrum of the free surface of shallow turbulent flows over a rough boundary," *Phys. Fluids*, vol. 28, no. 10, Oct. 2016, Art. no. 105105.

[37] K. F. Warnick and W. C. Chew, "Numerical simulation methods for rough surface scattering," *Waves Random Media*, vol. 11, no. 1, pp. R1–R30, Jan. 2001.

[38] Y. He, G. Wu, H. Mao, H. Chen, J. Lin, and G. Dong, "An experimental study on nonlinear wave dynamics for freak waves over an uneven bottom," *Frontiers Mar. Sci.*, vol. 10, pp. 1–13, Mar. 2023.

[39] S. B. Park, S. Y. Shin, D. G. Shin, H. Park, K. H. Jung, S. B. Suh, J. Lee, S. J. Lee, and H. S. Kim, "Experimental study of wave transmission and drift velocity using freely floating synthetic ice floes," *Ocean Eng.*, vol. 251, May 2022, Art. no. 111058.

[40] Z. Huang and W. Zhang, "An experimental study of effects of water depth on wave scattering and motion responses of a moored floating breakwater in regular waves," in *Proc. Int. Conf. Offshore Mech. Arctic Eng.*, vol. 6, Jan. 2011, pp. 411–418.

[41] M. Perlin, W. Choi, and Z. Tian, "Breaking waves in deep and intermediate waters," *Annu. Rev. Fluid Mech.*, vol. 45, no. 1, pp. 115–145, Jan. 2013.

[42] W. K. Melville and P. Matusov, "Distribution of breaking waves at the ocean surface," *Nature*, vol. 417, no. 6884, pp. 58–63, May 2002.

[43] M. Ryabkova, V. Karaev, J. Guo, and Y. Titchenko, "A review of wave spectrum models as applied to the problem of radar probing of the sea surface," *J. Geophys. Res., Oceans*, vol. 124, no. 10, pp. 7104–7134, Oct. 2019.

[44] G. L. Mellor, M. A. Donelan, and L.-Y. Oey, "A surface wave model for coupling with numerical ocean circulation models," *J. Atmos. Ocean. Technol.*, vol. 25, no. 10, pp. 1785–1807, Oct. 2008.

[45] Q. Liu, A. Babanin, Y. Fan, S. Zieger, C. Guan, and I.-J. Moon, "Numerical simulations of ocean surface waves under hurricane conditions: Assessment of existing model performance," *Ocean Model.*, vol. 118, pp. 73–93, Oct. 2017.

[46] D. Chalikov, "High-resolution numerical simulation of surface wave development under the action of wind," in *Geophysics and Ocean Waves Studies*. London, U.K.: IntechOpen, Mar. 2021.

[47] W.-W. Ding, W.-Z. Yue, S.-W. Sheng, J.-P. Wu, and Z.-J. Zou, "Numerical and experimental study on the Bragg reflection of water waves by multiple vertical thin plates," *J. Mar. Sci. Eng.*, vol. 10, no. 10, p. 1464, Oct. 2022.

[48] J. V. Toporkov and G. S. Brown, "Numerical simulations of scattering from time-varying, randomly rough surfaces," *IEEE Trans. Geosci. Remote Sens.*, vol. 38, no. 4, pp. 1616–1625, Jul. 2000.

[49] T. M. Elfouhaily and J. T. Johnson, "A new model for rough surface scattering," *IEEE Trans. Geosci. Remote Sens.*, vol. 45, no. 7, pp. 2300–2308, Jul. 2007.

[50] G. Xu, S. Zhang, and W. Shi, "Instantaneous prediction of irregular ocean surface wave based on deep learning," *Ocean Eng.*, vol. 267, Jan. 2023, Art. no. 113218.

[51] C. P. Cummins, G. T. Scarlett, and C. Windt, "Numerical analysis of wave–structure interaction of regular waves with surface-piercing inclined plates," *J. Ocean Eng. Mar. Energy*, vol. 8, no. 1, pp. 99–115, Nov. 2021.

[52] I. H. Shahrezaei and H.-C. Kim, "SAR marginal ice zone surface roughness visualization and electromagnetic interaction investigation based on sea state conditions," in *Proc. 7th Asia–Pacific Conf. Synth. Aperture Radar (APSAR)*, Bali, Indonesia, Nov. 2021, pp. 1–4.

[53] D. Vandemark, B. Chapron, T. Elfouhaily, and J. W. Campbell, "Impact of high-frequency waves on the ocean altimeter range bias," *J. Geophys. Res., Oceans*, vol. 110, no. C11, pp. 1–12, Nov. 2005.

[54] H. Jiang, H. Zheng, and L. Mu, "Improving altimeter wind speed retrievals using ocean wave parameters," *IEEE J. Sel. Topics Appl. Earth Observ. Remote Sens.*, vol. 13, pp. 1917–1924, 2020.

[55] E. J. Walsh, M. L. Banner, J. H. Churnside, J. A. Shaw, D. C. Vandemark, C. W. Wright, J. B. Jensen, and S. Lee, "Visual demonstration of three-scale sea-surface roughness under light wind conditions," *IEEE Trans. Geosci. Remote Sens.*, vol. 43, no. 8, pp. 1751–1762, Aug. 2005.

[56] D. Chalikov, "Numerical modeling of surface wave development under the action of wind," *Ocean Sci.*, vol. 14, no. 3, pp. 453–470, Jun. 2018.

[57] R. Tao, Y. Li, X. Bai, and A. Waheed, "Fractional weierstrass model for rough ocean surface and analytical derivation of its scattered field in a closed form," *IEEE Trans. Geosci. Remote Sens.*, vol. 50, no. 10, pp. 3627–3639, Oct. 2012.

[58] V. G. Irisov, "Radiometric model of the sea surface in the presence of currents," *IEEE Trans. Geosci. Remote Sens.*, vol. 45, no. 7, pp. 2116–2121, Jul. 2007.

[59] P. A. Hwang, "Impact on sea-surface electromagnetic scattering and emission modeling of recent progress on the parameterization of ocean surface roughness, drag coefficient, and whitecap coverage in high wind conditions," *IEEE J. Sel. Topics Appl. Earth Observ. Remote Sens.*, vol. 13, pp. 1879–1887, 2020.

[60] A. G. Voronovich and V. U. Zavorotny, "Full-polarization modeling of monostatic and bistatic radar scattering from a rough sea surface," *IEEE Trans. Antennas Propag.*, vol. 62, no. 3, pp. 1362–1371, Mar. 2014.

[61] G. Wu, L. Han, and L. Zhang, "Numerical simulation and backscattering characteristics of freak waves based on JONSWAP spectrum," *Frontiers Mar. Sci.*, vol. 9, pp. 1–13, May 2022.

[62] J. T. Johnson, R. J. Burkholder, J. V. Toporkov, D. R. Lyzenga, and W. J. Plant, "A numerical study of the retrieval of sea surface height profiles from low grazing angle radar data," *IEEE Trans. Geosci. Remote Sens.*, vol. 47, no. 6, pp. 1641–1650, Jun. 2009.

[63] I. H. Shahrezaei and H.-C. Kim, "A novel SAR fractal roughness modeling of complex random polar media and textural synthesis based on a numerical scattering distribution function processing," *IEEE J. Sel. Topics Appl. Earth Observ. Remote Sens.*, vol. 14, pp. 7386–7409, 2021.

[64] D. Xie, K.-S. Chen, and X. Yang, "Effects of wind wave spectra on radar backscatter from sea surface at different microwave bands: A numerical study," *IEEE Trans. Geosci. Remote Sens.*, vol. 57, no. 9, pp. 6325–6334, Sep. 2019.

[65] R. Sofiani, H. Heidar, and M. Kazerooni, "A smart meshing technique to speed up radar cross-section calculation of very large random rough surfaces," *J. Electromagn. Waves Appl.*, vol. 29, no. 7, pp. 941–952, Apr. 2015.

[66] N. Bi, J. Qin, and T. Jiang, "Partition detection and location of a Kelvin wake on a 2-D rough sea surface by feature selective validation," *IEEE Access*, vol. 6, pp. 16345–16352, 2018.

[67] Y. Zhang and L. Jiang, "A novel data-driven scheme for the ship wake identification on the 2-D dynamic sea surface," *IEEE Access*, vol. 8, pp. 69593–69600, 2020.

[68] N. J. M. Laxague, M. Curcic, J.-V. Björkqvist, and B. K. Haus, "Gravity-capillary wave spectral modulation by gravity waves," *IEEE Trans. Geosci. Remote Sens.*, vol. 55, no. 5, pp. 2477–2485, May 2017.

[69] N. J. M. Laxague, C. J. Zappa, D. A. LeBel, and M. L. Banner, "Spectral characteristics of gravity-capillary waves, with connections to wave growth and microbreaking," *J. Geophys. Res., Oceans*, vol. 123, no. 7, pp. 4576–4592, Jul. 2018.

[70] F. Fois, P. Hoogeboom, F. Le Chevalier, and A. Stoffelen, "An investigation on sea surface wave spectra and approximate scattering theories," in *Proc. IEEE Geosci. Remote Sens. Symp.*, Quebec City, QC, Canada, Jul. 2014, pp. 4366–4369.

[71] J.-L. Jou, W.-S. Lo, and L. I, "Rogue waves associated with resonant slow sloshing waves spontaneously excited in wind-driven water wave turbulence," *Phys. Fluids*, vol. 32, no. 12, Dec. 2020, Art. no. 122120.

[72] J. Wu, X. Hao, and L. Shen, "An improved adjoint-based ocean wave reconstruction and prediction method," *Flow*, vol. 2, p. E2, Jan. 2022.

[73] Y. Hou, B. Wen, C. Wang, and Y. Tian, "Numerical and experimental study on backscattering Doppler characteristics from 2-D nonlinear sealike surface at low grazing angle," *IEEE Trans. Antennas Propag.*, vol. 68, no. 2, pp. 1055–1065, Feb. 2020.

[74] S.-M. Lee, A. J. Gasiewski, and B.-J. Sohn, "Influences of two-scale roughness parameters on the ocean surface emissivity from satellite passive microwave measurements," *IEEE Trans. Geosci. Remote Sens.*, vol. 60, pp. 1–12, 2022, Art. no. 4204112,

[75] J. Prendergast, M. Li, and W. Sheng, "A study on the effects of wave spectra on wave energy conversions," *IEEE J. Ocean. Eng.*, vol. 45, no. 1, pp. 271–283, Jan. 2020.

[76] M. Al-Ani and M. Belmont, "On fully describing the probability distribution of quiescent periods from sea spectral density," *IEEE J. Ocean. Eng.*, vol. 46, no. 1, pp. 143–155, Jan. 2021.

[77] J. T. Johnson, J. V. Toporkov, and G. S. Brown, "A numerical study of backscattering from time-evolving sea surfaces: Comparison of hydrodynamic models," *IEEE Trans. Geosci. Remote Sens.*, vol. 39, no. 11, pp. 2411–2420, Nov. 2001.

[78] D. Nie, M. Zhang, W. Jiang, and J. Zhao, "Spectral investigation of Doppler signals from surfaces with a mixture of wind wave and swell," *IEEE Geosci. Remote Sens. Lett.*, vol. 14, no. 8, pp. 1353–1357, Aug. 2017.

[79] P.-B. Wei, M. Zhang, D. Nie, and Y.-C. Jiao, "Improvement of SSA approach for numerical simulation of sea surface scattering at high microwave bands," *Remote Sens.*, vol. 10, no. 7, p. 1021, Jun. 2018.

[80] A. Zapevalov, K. Pokazeev, and T. Chaplina, "Simulation of the sea surface for remote sensing," in *Springer Oceanography*. Cham, Switzerland: Springer, 2021.

[81] Y. Liu, M.-Y. Su, X.-H. Yan, and W. T. Liu, "The mean-square slope of ocean surface waves and its effects on radar backscatter," *J. Atmos. Ocean. Technol.*, vol. 17, no. 8, pp. 1092–1105, Aug. 2000.

[82] D. Riccio and G. Ruello, "Synthesis of fractal surfaces for remote-sensing applications," *IEEE Trans. Geosci. Remote Sens.*, vol. 53, no. 7, pp. 3803–3814, Jul. 2015.

[83] C. Wang, Y. Tian, J. Yang, H. Zhou, B. Wen, X. Xu, and W. Huang, "Validation and intercomparison of sea state parameter estimation with multisensors for OSMAR-S high-frequency radar," *IEEE Trans. Instrum. Meas.*, vol. 69, no. 10, pp. 7552–7565, Oct. 2020.

[84] Y. Zeng, H. Zhou, Y. Lai, and B. Wen, "Wind-direction mapping with a modified wind spreading function by broad-beam high-frequency radar," *IEEE Geosci. Remote Sens. Lett.*, vol. 15, no. 5, pp. 679–683, May 2018.

[85] I. H. Shahrezaei, H.-C. Kim, and T.-B. Chae, "Ultra-high resolution KOMPSAT-5 SAR sea-ice random radiometric anomaly formulation based on hybrid domain texture decomposition," in *Proc. Int. Conf. Radar, Antenna, Microw., Electron., Telecommun. (ICRAMET)*, Tangerang, Indonesia, Nov. 2020, pp. 325–330.

[86] T. Wang and C. Tong, "An improved facet-based TSM for electromagnetic scattering from ocean surface," *IEEE Geosci. Remote Sens. Lett.*, vol. 15, no. 5, pp. 644–648, May 2018.

[87] P. A. Hwang and T. L. Ainsworth, "L-band ocean surface roughness," *IEEE Trans. Geosci. Remote Sens.*, vol. 58, no. 6, pp. 3988–3999, Jun. 2020.

[88] I. H. Shahrezaei and H.-C. Kim, "Numerical SAR SEA-ICE modeling and surface backscattering properties based on energy scattering distribution computation," in *Proc. IEEE Int. Geosci. Remote Sens. Symp.*, Kuala Lumpur, Malaysia, Jul. 2022, pp. 4571–4574.

[89] L. Cavaleri, "Wave modelling—The state of the art," *Prog. Oceanogr.*, vol. 75, no. 4, pp. 603–674, Dec. 2007.

[90] Q. Jiang, Y. Xu, H. Sun, L. Wei, L. Yang, Q. Zheng, H. Jiang, X. Zhang, and C. Qian, "Wind-generated gravity waves retrieval from high-resolution 2-D maps of sea surface elevation by airborne interferometric altimeter," *IEEE Geosci. Remote Sens. Lett.*, vol. 19, pp. 1–5, 2022.

[91] M. Amani, A. Ghorbanian, M. Asgarimehr, B. Yekkehkhany, A. Moghimi, S. Jin, A. Naboureh, F. Mohseni, S. Mahdavi, and N. F. Layegh, "Remote sensing systems for ocean: A review (Part 1: Passive systems)," *IEEE J. Sel. Topics Appl. Earth Observ. Remote Sens.*, vol. 15, pp. 210–234, 2022.

[92] M. Amani, F. Mohseni, N. F. Layegh, M. E. Nazari, F. Fatolazadeh, A. Salehi, S. A. Ahmadi, H. Ebrahimy, A. Ghorbanian, S. Jin, S. Mahdavi, and A. Moghimi, "Remote sensing systems for ocean: A review (Part 2: Active systems)," *IEEE J. Sel. Topics Appl. Earth Observ. Remote Sens.*, vol. 15, pp. 1421–1453, 2022.

[93] I. G. Rizaev, O. Karakus, S. J. Hogan, and A. Achim, "Modeling and SAR imaging of the sea surface: A review of the state-of-the-art with simulations," *ISPRS J. Photogramm. Remote Sens.*, vol. 187, pp. 120–140, May 2022.

[94] T. Elfouhaily, B. Chapron, K. Katsaros, and D. Vandemark, "A unified directional spectrum for long and short wind-driven waves," *J. Geophys. Res., Oceans*, vol. 102, no. C7, pp. 15781–15796, Jul. 1997.

[95] S. R. Massel, "On the geometry of ocean surface waves," *Oceanologia*, vol. 53, no. 2, pp. 521–548, Jun. 2011.

[96] L. Yuguang, Y. Xiao-Hai, and S. Ming-Yang, "Directional spectrum of wind waves: Part II—Comparison and confirmation," *J. Ocean Univ. Qingdao*, vol. 2, no. 1, pp. 13–23, Apr. 2003.

[97] P. A. Hwang and Y. Fan, "Low-frequency mean square slopes and dominant wave spectral properties: Toward tropical cyclone remote sensing," *IEEE Trans. Geosci. Remote Sens.*, vol. 56, no. 12, pp. 7359–7368, Dec. 2018.

[98] A. R. Hayslip, J. T. Johnson, and G. R. Baker, "Further numerical studies of backscattering from time-evolving nonlinear sea surfaces," *IEEE Trans. Geosci. Remote Sens.*, vol. 41, no. 10, pp. 2287–2293, Oct. 2003.

[99] S.-M. Lee and A. J. Gasiewski, "A physically based two-scale ocean surface emissivity model tuned to WindSat and SSM/I polarimetric brightness temperatures," *IEEE Trans. Geosci. Remote Sens.*, vol. 60, pp. 1–23, 2022, Art. no. 4205523.

[100] S. S. Abeysekera, "Investigation of nonlinear interactions in ocean swell waves using the reduced bispectrum," *IEEE J. Ocean. Eng.*, vol. 24, no. 3, pp. 312–322, Jul. 1999.

[101] I. R. Young, "The form of the asymptotic depth-limited wind-wave spectrum: Part II—The wavenumber spectrum," *Coastal Eng.*, vol. 57, no. 1, pp. 30–40, Jan. 2010.

[102] Y. Zhao, X.-F. Yuan, M. Zhang, and H. Chen, "Radar scattering from the composite ship-ocean scene: Facet-based asymptotical model and specular reflection weighted model," *IEEE Trans. Antennas Propag.*, vol. 62, no. 9, pp. 4810–4815, Sep. 2014.

[103] Y. Miao, X. Dong, M. A. Bourassa, and D. Zhu, "Effects of ocean wave directional spectra on Doppler retrievals of ocean surface current," *IEEE Trans. Geosci. Remote Sens.*, vol. 60, pp. 1–12, 2022.

[104] R. D. Montoya, A. O. Arias, J. C. Ortiz Royero, and F. J. Ocampo-Torres, "A wave parameters and directional spectrum analysis for extreme winds," *Ocean Eng.*, vol. 67, pp. 100–118, Jul. 2013.

[105] S. Zhang and J. Zhang, "A new approach to estimate directional spreading parameters of a cosine-2s model," *J. Atmos. Ocean. Technol.*, vol. 23, no. 2, pp. 287–301, Feb. 2006.

[106] S. L. Durden and J. F. Vesecky, "A numerical study of the separation wavenumber in the two-scale scattering approximation (ocean surface radar backscatter)," *IEEE Trans. Geosci. Remote Sens.*, vol. 28, no. 2, pp. 271–272, Mar. 1990.

[107] J. T. Johnson, R. T. Shin, J. Au Kong, L. Tsang, and K. Pak, "A numerical study of the composite surface model for ocean backscattering," *IEEE Trans. Geosci. Remote Sens.*, vol. 36, no. 1, pp. 72–83, Jan. 1998.

[108] I. PopStefanija, C. W. Fairall, and E. J. Walsh, "Mapping of directional ocean wave spectra in hurricanes and other environments," *IEEE Trans. Geosci. Remote Sens.*, vol. 59, no. 11, pp. 9007–9020, Nov. 2021.

[109] H. Mitsuyasu, F. Tasai, T. Suhara, S. Mizuno, M. Ohkusu, T. Honda, and K. Rikiishi, "Observations of the directional spectrum of ocean WavesUsing a cloverleaf buoy," *J. Phys. Oceanogr.*, vol. 5, no. 4, pp. 750–760, Oct. 1975.

[110] D. E. Hasselmann, M. Dunckel, and J. A. Ewing, "Directional wave spectra observed during JONSWAP 1973," *J. Phys. Oceanogr.*, vol. 10, no. 8, pp. 1264–1280, Aug. 1980.

[111] M. A. Donlen, J. Hamilton, and W. H. Hui, "Directional spectra of wind-generated ocean waves," *Phil. Trans. Roy. Soc. London. Ser. A, Math. Phys. Sci.*, vol. 315, no. 1534, pp. 509–562, Sep. 1534.

[112] K. C. Ewans, "Observations of the directional spectrum of fetch-limited waves," *J. Phys. Oceanogr.*, vol. 28, no. 3, pp. 495–512, Mar. 1998.

[113] M. A. Bourassa et al., "Remotely sensed winds and wind stresses for marine forecasting and ocean modeling," *Frontiers Mar. Sci.*, vol. 6, Aug. 2019, Art. no. 437064.

[114] H. Pan, W. Zhang, W. Jiang, P. Wang, J. Yang, and X. Zhang, "Roughness change analysis of sea surface from visible images by fractals," *IEEE Access*, vol. 8, pp. 78519–78529, 2020.

[115] D. Myrhaug, B. J. Leira, and W. Chai, "Application of a sea surface roughness formula using joint statistics of significant wave height and spectral wave steepness," *J. Ocean Eng. Mar. Energy*, vol. 6, no. 1, pp. 91–97, Feb. 2020.

[116] K. R. Prakash, V. Pant, and T. Nigam, "Effects of the sea surface roughness and sea spray-induced flux parameterization on the simulations of a tropical cyclone," *J. Geophys. Res., Atmos.*, vol. 124, no. 24, pp. 14037–14058, Dec. 2019.

[117] D. Yang, C. Meneveau, and L. Shen, "Dynamic modelling of sea-surface roughness for large-eddy simulation of wind over ocean wavefield," *J. Fluid Mech.*, vol. 726, pp. 62–99, May 2013.

[118] M. Curcic and B. K. Haus, "Revised estimates of ocean surface drag in strong winds," *Geophys. Res. Lett.*, vol. 47, no. 10, May 2020, Art. no. e2020GL087647.

[119] F. Nouguier, C.-A. Guerin, and G. Soriano, "Analytical techniques for the Doppler signature of sea surfaces in the microwave regime—II: Nonlinear surfaces," *IEEE Trans. Geosci. Remote Sens.*, vol. 49, no. 12, pp. 4920–4927, Dec. 2011.

[120] C.-S. Chae and J. T. Johnson, "A study of interferometric phase statistics and accuracy for sea surface height retrievals from numerically simulated low-grazing-angle backscatter data," *IEEE Trans. Geosci. Remote Sens.*, vol. 49, no. 11, pp. 4580–4587, Nov. 2011.

[121] A. P. Wijaya and E. van Groesen, "Determination of the significant wave height from shadowing in synthetic radar images," *Ocean Eng.*, vol. 114, pp. 204–215, Mar. 2016.

[122] I. H. Shahrezaei and H.-C. Kim, "A monostatic forward-looking staring spotlight SAR raw data generation and hybrid-domain image formation modifications based on extended azimuth nonlinear chirp scaling autofocusing," *IEEE Trans. Aerosp. Electron. Syst.*, vol. 59, no. 3, pp. 2329–2358, Jun. 2023.

[123] I. H. Shahrezaei and H.-C. Kim, "Fractal analysis and texture classification of high-frequency multiplicative noise in SAR sea-ice images based on a Transform- domain image decomposition method," *IEEE Access*, vol. 8, pp. 40198–40223, 2020.
[124] C. Pohl and J. van Genderen, *Remote Sensing Image Fusion*. Boca Raton, FL, USA: CRC Press, 2016.
[125] J. Fu, W. Li, J. Du, and B. Xiao, "Multimodal medical image fusion via Laplacian pyramid and convolutional neural network reconstruction with local gradient energy strategy," *Comput. Biol. Med.*, vol. 126, Nov. 2020, Art. no. 104048.
[126] X. Li, F. Zhou, H. Tan, W. Zhang, and C. Zhao, "Multimodal medical image fusion based on joint bilateral filter and local gradient energy," *Inf. Sci.*, vol. 569, pp. 302–325, Aug. 2021.
[127] W. Zhang, L. Jiao, Y. Li, Z. Huang, and H. Wang, "Laplacian feature pyramid network for object detection in VHR optical remote sensing images," *IEEE Trans. Geosci. Remote Sens.*, vol. 60, pp. 1–14, 2022, Art. no. 5604114.
[128] J. Kim, J. K. Lee, and K. M. Lee, "Accurate image super-resolution using very deep convolutional networks," in *Proc. IEEE Conf. Comput. Vis. Pattern Recognit. (CVPR)*, Las Vegas, NV, USA, Jun. 2016, pp. 1646–1654.
[129] Y. Du, J. Liu, W. Song, Q. He, and D. Huang, "Ocean eddy recognition in SAR images with adaptive weighted feature fusion," *IEEE Access*, vol. 7, pp. 152023–152033, 2019.
[130] C. R. D. Macedo and J. A. Lorenzzetti, "Numerical simulations of SAR microwave imaging of the Brazil current surface front," *Brazilian J. Oceanogr.*, vol. 63, no. 4, pp. 481–496, Dec. 2015.
[131] Z. Lin, T. A. A. Adcock, and M. L. McAllister, "Estimating ocean wave directional spreading using wave following buoys: A comparison of experimental buoy and gauge data," *J. Ocean Eng. Mar. Energy*, vol. 8, no. 1, pp. 83–97, Nov. 2021.
[132] H.-L. Liu, "Quantifying gravity wave forcing using scale invariance," *Nature Commun.*, vol. 10, no. 1, pp. 1–12, Jun. 2019.
[133] T. Hara and S. E. Belcher, "Wind forcing in the equilibrium range of wind-wave spectra," *J. Fluid Mech.*, vol. 470, pp. 223–245, Oct. 2002.
[134] J. Klinke and B. Jaehne, "Two-dimensional wave number spectra of short wind waves: Results from wind-wave facilities and extrapolation to the ocean," *Proc. SPIE*, vol. 1792, pp. 245–257, Dec. 1992.
[135] V. Kudryavtsev, M. Yurovskaya, and B. Chapron, "Self-similarity of surface wave developments under tropical cyclones," *J. Geophys. Res., Oceans*, vol. 126, no. 4, pp. 1–31, Apr. 2021.
[136] H. Naeser, "The capillary waves' contribution to wind-wave generation," *Fluids*, vol. 7, no. 2, p. 73, Feb. 2022.
[137] H. Mitsuyasu, "Measurement of the high-frequency spectrum of ocean surface waves," *J. Phys. Oceanogr.*, vol. 7, no. 6, pp. 882–891, Nov. 1977.
[138] W. J. Plant, "Short wind waves on the ocean: Wavenumber-frequency spectra," *J. Geophys. Res., Oceans*, vol. 120, no. 3, pp. 2147–2158, Mar. 2015.
[139] P. P. Sullivan, M. L. Banner, R. P. Morison, and W. L. Peirson, "Impacts of wave age on turbulent flow and drag of steep waves," *Proc. IUTAM*, vol. 26, pp. 174–183, Jan. 2018.
[140] Y. Wan, R. Qu, Y. Dai, and X. Zhang, "Research on the applicability of the e spectrum and PM spectrum as the first guess spectrum of SAR wave spectrum inversion," *IEEE Access*, vol. 8, pp. 169082–169095, 2020.
[141] Y. Wang, Y. Zhang, H. Li, and G. Chen, "Doppler spectrum of microwave SAR signals from two-dimensional time-varying sea surface," *J. Electromagn. Waves Appl.*, vol. 30, no. 10, pp. 1265–1276, Jun. 2016.
[142] A. S. Zapevalov, "Anisotropy of sea surface roughness formed by waves of different scales," in *Processes in GeoMedia—Volume IV*. Cham, Switzerland: Springer, Nov. 2021, pp. 277–284.
[143] J. A. Smith, "Wave–Current interactions in finite depth," *J. Phys. Oceanogr.*, vol. 36, no. 7, pp. 1403–1419, Jul. 2006.
[144] A. D. Jones, A. J. Duncan, A. L. Maggi, D. W. Bartel, and A. Zinoviev, "A detailed comparison between a small-slope model of acoustical scattering from a rough sea surface and stochastic modeling of the coherent surface loss," *IEEE J. Ocean. Eng.*, vol. 41, no. 3, pp. 689–708, Jul. 2016.
[145] D. Hauser, "Measuring and analysing the directional spectra of ocean waves," Office Off. Publications Eur. Communities, COST, 2005, p. 485.
[146] Y. Goda, "A comparative review on the functional forms of directional wave spectrum," *Coastal Eng. J.*, vol. 41, no. 1, pp. 1–20, Mar. 1999.
[147] M. I. Skolnik, "Sea clutter," in *Radar Handbook*, vol. 1999. New York, NY, USA: McGraw-Hill, 1999, p. 13.
[148] I. H. Shahrezaei and H.-C. Kim, "Resolutional analysis of multiplicative high-frequency speckle noise based on SAR spatial de-speckling filter implementation and selection," *Remote Sens.*, vol. 11, no. 9, p. 1041, May 2019.
[149] I. H. Shahrezaei, M. Kazerooni, and M. Fallah, "A complex target terrain SAR raw data generation and evaluation based on inversed equalized hybrid-domain algorithm processing," *Waves Random Complex Media*, vol. 27, no. 1, pp. 47–66, Jun. 2016.
[150] X. Luo, G. Fu, J. Yang, Y. Cao, and Y. Cao, "Multi-modal image fusion via deep Laplacian pyramid hybrid network," *IEEE Trans. Circuits Syst. Video Technol.*, vol. 33, no. 12, pp. 7354–7369, Dec. 2023, doi: 10.1109/TCSVT.2023.3281462.
[151] A. Akl, C. Yaacoub, M. Donias, J.-P. Da Costa, and C. Germain, "Texture synthesis using the structure tensor," *IEEE Trans. Image Process.*, vol. 24, no. 11, pp. 4082–4095, Nov. 2015.
[152] V. B. S. Prasath, R. Pelapur, G. Seetharaman, and K. Palaniappan, "Multiscale structure tensor for improved feature extraction and image regularization," *IEEE Trans. Image Process.*, vol. 28, no. 12, pp. 6198–6210, Dec. 2019.

IMAN HEIDARPOUR SHAHREZAEI (Member, IEEE) was born in Isfahan, Iran, in 1985. He received the B.Sc. and M.Sc. degrees in electrical and telecommunication engineering from the University of Urmia, Urmia, Iran, in 2007 and 2011, respectively, and the Ph.D. degree in electrical and telecommunication engineering from the Malek-Ashtar University of Technology (MUT), Tehran, Iran, in 2017, specialized in electromagnetic fields and waves. Since December 2018, he has been a Postdoctoral Researcher with Korea Polar Research Institute (KOPRI), Center for Remote Sensing and Geospatial Information Systems (GIS). The center consists of numerical remote sensing modeling and satellite signal processing. His current research interests include radar remote sensing, microwave imaging, modeling in remote sensing, image analysis and data fusion, radiation and backscattering theories, and the development of synthetic aperture RADAR (SAR) sensors, including the image formation algorithms.

HYUN-CHEOL KIM (Member, IEEE) received the Ph.D. degree in earth and environmental sciences with a major in satellite oceanography from Seoul National University, Seoul, Republic of Korea, in 2006. Since 2007, he has been with Korea Polar Research Institute (KOPRI) using satellite and unmanned aerial vehicle (UAV) remote sensing data for the purpose of Arctic and Antarctic research. He established a remote sensing group in KOPRI, in 2016. He leads the Center for Remote Sensing and Geospatial Information Systems (GIS) as the Director. The center consists of many specialized fields of satellite remote sensing, ocean color, SAR, passive microwave, optical remote sensing, and UAVs. The group mainly studies the cryosphere for climate change using remote sensing data. Notably, he is the First Scientist to use KOMPSAT (Korea Multipurpose Satellite) for polar science. He is also actively involved in many international programs. He was a recipient of a Korea Prime Ministerial Citation for Excellence in Ocean Science, in 2019.